JACS
JOURNAL OF THE AMERICAN CHEMICAL SOCIETY

Article

Confinement-Driven Photophysics in Cages, COFs, MOFs, and DNA

Ekaterina A. Dolgopolova, Anna A Berseneva, Martín S. Faillace, Otega A. Ejegbavwo, Gabrielle A. Leith, Seok W. Choi, Haley N. Gregory, Allison M Rice, Mark D. Smith, Maksymilian Chruszcz, Sophya Garashchuk, Karthikeyan Mythreye, and Natalia B. Shustova

J. Am. Chem. Soc., **Just Accepted Manuscript** • DOI: 10.1021/jacs.9b13505 • Publication Date (Web): 19 Feb 2020

Just Accepted

is published by the American Chemical Society. 1155 Sixteenth Street N.W., Washington, DC 20036

Confinement-Driven Photophysics in Cages, COFs, MOFs, and DNA

Ekaterina A. Dolgopolova,[a] Anna A. Berseneva,[a] Martín S. Faillace,[b] Otega A. Ejegbavwo,[a] Gabrielle A. Leith,[a] Seok W. Choi,[a] Haley N. Gregory,[a] Allison M. Rice,[a] Mark D. Smith,[a] Maksymilian Chruszcz,[a] Sophya Garashchuk,[a] Karthikeyan Mythreye,[a] and Natalia B. Shustova [a*]

[a] Department of Chemistry and Biochemistry, University of South Carolina, Columbia, South Carolina 29208, United States
[b] INFIQC-UNC, CONICET, Departamento de Fisicoquímica, Facultad de Ciencias Químicas, Universidad Nacional de Córdoba, Córdoba, X5000HUA, Argentina

ABSTRACT: Photophysics tunability through alteration of framework aperture (metal-organic framework (MOF) = variable; guest = constant) was probed for the first time in comparison with previously explored concepts (MOF = constant; guest = variable). In particular, analysis of the confinement effect on a photophysical response of integrated Cl-BI (5-(3-chlorobenzylidene)-2,3-dimethyl-3,5-dihydro-4*H*-imidazol-4-one) chromophore allowed us to establish a photophysics-aperture relationship. To shed light on the observed correlation, the framework confined environment was replicated using a molecular cage, $Pd_6(TPT)_4$ (TPT = 2,4,6-tri(pyridin-4-yl)-1,3,5-triazine); thus, allowing for utilization of crystallography, spectroscopy, and theoretical simulations to reveal the effect a confined space has on the chromophore molecular conformation (including disruption of strong hydrogen bonding and novel conformer formation) and any associated changes on a photophysical response. Furthermore, the chosen Cl-*o*HBI@$Pd_6(TPT)_4$ (Cl-*o*HBI = 5-(5-chloro-2-hydroxybenzylidene)-2,3-dimethyl-3,5-dihydro-4*H*-imidazol-4-one, chromophore) system was applied as a tool for targeted cargo delivery of a chromophore to the confined space of DNA, and resulted in promotion of chromophore-DNA interactions through a well-established intercalation mechanism. Moreover, the developed principles were applied towards utilizing a 5-(4-hydroxybenzylidene)-3,5-dihydro-4*H*-imidazol-4-one (HBI) chromophore as a fluorescent probe on the example of macrophage cells. For the first time, suppression of non-radiative decay pathways of a chromophore was tested by anchoring the chromophore to a framework metal node, portending a potential avenue to develop an alternative to natural biomarkers. Overall, these studies are among the first attempts to demonstrate the unrevealed potential of a confined scaffold environment for tailoring material photophysical response.

INTRODUCTION

Confined environment can impose significant constrictions on chromophore behavior resulting in changes in structure/conformation, and as a result, photophysical response.[1–13] Such confinement-dependent photophysics could be a complementary strategy to the known concept of fluorescent response modulation through chromophore chemical modifications, and therefore, could potentially be applied towards hierarchical luminophore development.[4,14–19] Extended crystalline porous materials (e.g., metal- and covalent-organic frameworks (MOFs and COFs)) could influence guest chromophore emission through transformations in molecular conformation or separating chromophores, effectively preventing self-aggregation or quenching.[20,21] Infiltration of guest molecules inside porous matrices could allow for access to properties that are not traditionally accessible in the solid state or solution.[22–25] Multi-component integration can lead to desirable material properties that are uncharacteristic of the individual parts, i.e., an unrestricted chromophore within a host matrix (Scheme 1). Previously, most of the reported approaches focused on modification of the photophysical response of a whole system by utilizing a guest as a variable while the framework remains unchanged. This strategy very often requires precise chemical modification of components (i.e., synthesis of guest molecules with desirable properties or functionalization of the framework), which can be labor- and time-demanding. In contrast, a strategy for photophysical response modulation as a function of framework topology is still unexplored.

Scheme 1. Schematic representation of rigid scaffold induced changes on a molecular conformation and photophysical response of a chromophore (a rigid scaffold = MOF, COF, cage, and DNA studied in this work).

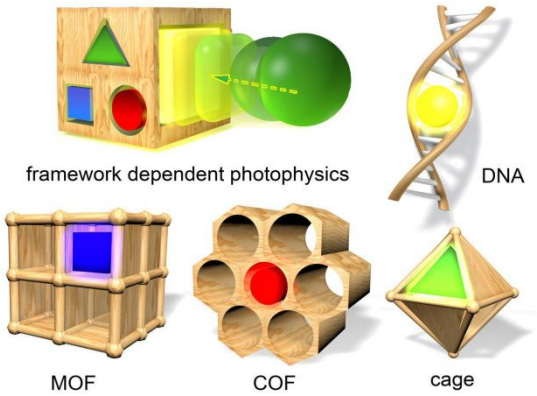

Therefore, in this work, we (i) elaborated on a novel concept that relies on systematic investigation of framework topology with different pore apertures (MOF = variable) while the

selected chromophore remains unchanged (guest = constant); (ii) performed the first attempt to establish a correlation between porous framework geometry and photophysical response of an embedded chromophore; (iii) shed light on the relationship between possible molecular conformation of a chromophore inside an artificial rigid scaffold and drastic changes in the photophysical profile using a molecular cage as a MOF truncated model; (iv) demonstrated that a confined environment can disrupt strong intramolecular hydrogen bonding leading to formation of novel conformers; (v) probed the chromophore interactions inside the confined space of DNA by utilizing a molecular cage as a tool for chromophore delivery; (vi) elucidated the mechanism of chromophore-DNA interactions; and finally, (viii) suppressed non-radiative decays of a chromophore through coordination to a metal node for the first time.

The discussion in this paper is organized in the following order: modulation of photophysics as a function of framework topology (MOF = variable, guest = constant, Figure 1); utilization of a molecular cage ($Pd_6(TPT)_4$) as a model system for establishing a correlation between the chromophore molecular conformation and photophysical response by X-ray studies and theoretical simulations; employment of the developed chromophore@cage system for studies of chromophore behavior within the confined space of DNA including experiments performed on macrophages cells; and investigation of metal node-chromophore interactions.

RESULTS AND DISCUSSION

For tuning the emission profile in host-guest systems (e.g., host = MOF, COF, or cage), a guest molecule is often used as a variable, while the host is used as a constant; i.e., different chromophores with distinct emission profiles immobilized in a framework serving as a porous scaffold (Figures 1a,c). Therefore, framework photoluminescence can be modulated as a function of a guest.[23,26–43] However, the concept of tailoring photophysical properties of a material as a function of chromophore molecular conformation imposed by the topology of the porous framework, such as MOF or COF, is still unexplored despite the great potential provided by framework modularity.[44,45] The presented work is the first step to probing this hypothesis and studying a possible correlation between the pore aperture and the photophysical response inside the confined space of a framework.

To explore the possibility of tunable chromophore conformation, we studied photophysical profiles of 5-(3-chlorobenzylidene)-2,3-dimethyl-3,5-dihydro-4*H*-imidazol-4-one chromophore (Cl-BI)[46,47] inside nine MOF motifs with varying pore apertures (Figure 1b). One of the criteria for the choice of a chromophore was the absence of functional group(s) that could interfere with a metal salt or linker, allowing for the chromophore incorporation during the solvothermal synthesis. Presence of the chlorine atom in the skeleton in the *meta* position on the phenyl ring promotes formation of distinct chromophore conformations due to the phenyl ring rotation. Moreover, Cl atom (with a relatively large Z number in comparison with light elements such as C, N, or H) will affect the scattering amplitude of X-rays that could facilitate the structure elucidation of the guest molecules inside the confined space of a framework. The choice of a MOF as a rigid host was based on the following criteria: (i) sufficient pore aperture for chromophore incorporation (from 11 to 19.5 Å); (ii) ability to preserve scaffold crystallinity after chromophore incorporation; (iii) presence of metal nodes consisting of d^0 and d^{10} metals to avoid fluorescence quenching, and (iv) absence of interference between host and guest emission profiles with only one exception of $Zr_6O_4(OH)_4(TPDC\text{-}NH_2)_6$ (**10**, $TPDC\text{-}NH_2^{2-}$ = 2′-amino-terphenyl-4,4′-dicarboxylate) as discussed below.

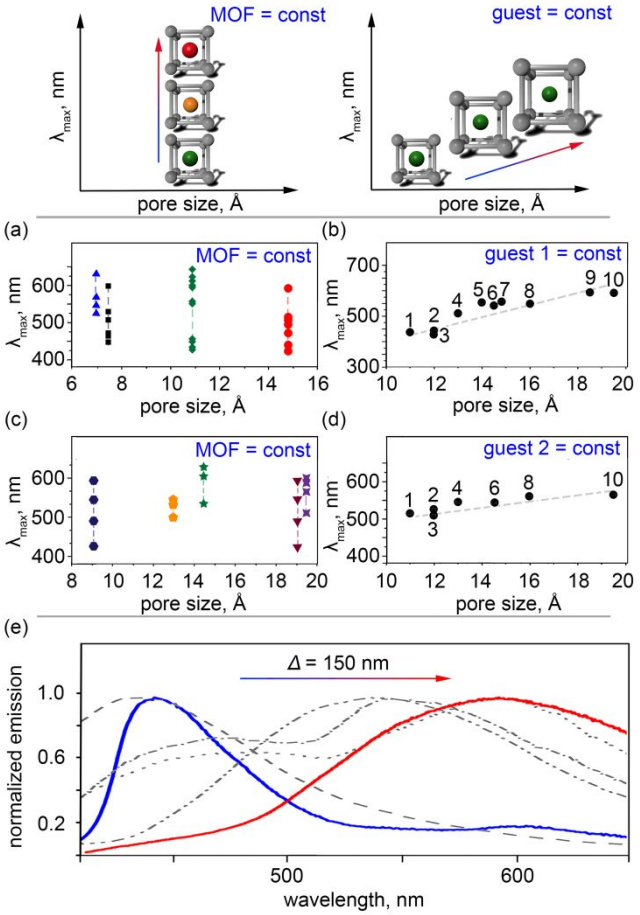

Figure 1. (*top*) Emission maxima of encapsulated chromophores as a function of: (*left*) a guest chromophore (MOF = constant, guest = variable), (*right*) a framework pore size (guest = constant, MOF = variable).
Dependence of the guest@MOF emission maximum as a function of the framework pore size:
(*a*) MOF = constant, guest = variable (literature analysis).[23,32,47,48]
(*b*) MOF = variable, guest = constant (this work).
(*c*) MOF = constant, guest = variable (literature analysis).[33–43]
(*d*) MOF = variable, guest = constant (literature analysis).[49]
(*e*) Normalized emission spectra of Cl-BI chromophore incorporated inside rigid scaffolds (this work).
The solid blue and red lines correspond to normalized emission of Cl-BI in the solid state and Cl-BI@9, respectively. Gray lines represent the observed trend in changes in fluorescence response of Cl-BI@MOF: Cl-BI@1 (- - -), Cl-BI@6 (-·-·-), Cl-BI@8 (-···-), and Cl-BI@10 (···). Guest 1 = Cl-BI; guest 2 = MeO-*o*HBI. An excitation wavelength of 350 nm was used to acquire all photoluminescence spectra in the solid state.

Integration of Cl-BI occurred in parallel with the framework synthesis itself, i.e., the corresponding metal salt, linker, and chromophore were heated simultaneously, resulting in the formation of Cl-BI@MOF, where MOF = $Zn_3(BTC)_2$ (**1**, BTC^{3-} = benzene-1,3,5-tricarboxylate),[50] $Zn_4O(BTB)_2$ (**2**, BTB^{3-} = benzene-1,3,5-tribenzoate),[51] $Zn_6(BTB)_4(BP)_3$ (**3**, BP = 4,4′-bipyridyl),[52] $Zr_6O_4(OH)_4(BDC)_6$ (**4**, BDC^{2-} =

terephthalate),[53] $Zn_4O(NDC)_3$ (**5**, NDC^{2-} = naphthalene-2,6-dicarboxylate),[54] $Zr_6O_4(OH)_4(BPDC)_6$ (**6**, $BPDC^{2-}$ = biphenyl-4,4′-dicarboxylate),[53] $Zn_2(DOBDC)$ (**7**, $DOBDC^{2-}$ = 2,5-dihydroxyterephthalate),[55] $Zr_6O_4(OH)_{10}(BTB)_2$ (**8**),[56] and $Zr_6O_4(OH)_4(TPDC\text{-}NH_2)_6$ (**10**).[53] Prepared Cl-BI@MOFs were thoroughly washed with *N,N*-dimethylformamide (DMF) to remove excess residual chromophore from the surface. Crystallographic studies confirmed preparation of the hosts as well as preservation of framework crystallinity (Figures S1–S9).

The comprehensive analysis of photoluminescence data for Cl-BI@MOFs revealed tunability of the emission maximum (λ_{max}) of Cl-BI incorporated inside a MOF (Figure 1e) in comparison with that in the solid state (λ_{max} = 443 nm, λ_{ex} = 350 nm). Indeed, a drastic shift of λ_{max} over 150 nm (0.7 eV) was detected when Cl-BI was integrated, for instance, inside **10** (Figure 1e) in comparison with that of the chromophore in the solid state. Attempts to correlate the observed Cl-BI@MOF behavior to that in solution revealed that, in contrast to changes in the Cl-BI@MOF emission maxima ($\Delta\lambda_{10}$= 150 nm), photophysical studies of Cl-BI in a variety of solvents demonstrated that $\Delta\lambda_{solvent}$ can be tuned only within 17 nm (Figure S13). A plethora of control experiments were also performed to confirm that the observed changes in emission are associated only with guest behavior and are not attributed to interactions with the solvent (Figures S10 and S13) or the MOF organic linkers (Figures S14–S17). In all of these experiments, no significant changes in emission profile of chromophore were observed leading to the hypothesis that a confined space of the framework could potentially affect emission profile of the guest, and therefore, we studied the possibility to correlate the Cl-BI@MOF emission maximum and framework pore size. Emission of all frameworks, with the exception of **10,** does not interfere with the chromophore emission maximum. In the latter case, our control experiments demonstrated that we can deconvolute photophysical properties of a chromophore molecule from a host (Figures S11 and S12), and as a result, this strategy was applied towards Cl-BI@**10** as well (see more details in the Supporting Information).

Analysis of photophysical data and framework geometry revealed a possible correlation between λ_{max} and pore size, i.e., an increase in pore size led to a bathochromic shift in the emission profile of the guest as shown in Figure 1b. Analysis of literature verified that the observed tendency is in line with the data previously reported for the 5-(2-hydroxy-5-methoxybenzylidene)-2,3-dimethyl-3,5-dihydro-4*H*-imidazol-4-one chromophore (MeO-*o*HBI) integrated in different MOFs as shown in Figure 1d.[49] Thus, the presented studies and literature analysis demonstrate the great potential of the proposed concept: emission response modulation of encapsulated guests as a function of framework pore aperture. Such a concept could potentially address issues associated with chromophore core derivatization traditionally necessary for emission tunability, especially in the near-infrared region.

To elucidate possible factors that led to the detected bathochromic shift, we employed single-crystal X-ray diffraction in combination with theoretical modeling. For the structural analysis, we utilized a $Pd_6(TPT)_4$ cage[57] (**9**, TPT = 2,4,6-tri(pyridin-4-yl)-1,3,5-triazine) as a truncated model of porous frameworks since our attempts to use the extended structures themselves inlcuding the previously employed $(ZnI_2)_3(TPT)_2$ framework[57] were not successful due to extensive disorder of the incorporated chromophores (a well-known problem in the MOF field).[58–62] The choice of this particular cage was determined by the fact that Cl-BI@**9** possesses the same λ_{max} in comparison with that of Cl-BI@**10** for which we detected the most drastic changes in emission. Furthermore, **9** possesses the similar pore size (~19 Å) compared to that of **10**. Thus, through utilization of **9**, we could probe the chromophore molecular conformation in the extended system **10** with the most drastic changes in λ_{max} crystallographically with the possibility to correlate the determined molecular conformation with an observed photophysical response through theoretical modeling.

Integration of the chromophore inside the cage was performed by simultaneously heating Cl-BI and $Pd_6(TPT)_4$ at 80 °C in D_2O. After cooling to room temperature and allowing the solvent to evaporate, crystals of Cl-BI@$Pd_6(TPT)_4$ were obtained that were suitable for single-crystal X-ray data collection (Figure S19). The structural analysis revealed that the chromophore conformation changed upon its incorporation inside the cage cavity compared to that in the solid state (Cl-BI*, Figure 2). The difference between immobilized Cl-BI* and Cl-BI observed in the solid state is the position of the chlorine atom relative to the oxygen atom, i.e., the oxygen and chlorine atoms on the imidazolone and phenyl rings, respectively, are pointing in opposite directions in the Cl-BI* molecule as shown in Figure 2. However, the isolated molecular conformation (Cl-BI*) is not predominant for 5-(4-hydroxybenzylidene)-3,5-dihydro-4*H*-imidazol-4-one (HBI)-based chromophores. For instance, analysis of 163 known crystal structures containing HBI-based molecules demonstrated that less than 5% of them possess the unique molecular conformation of Cl-BI* (Figure S21). To shed light on chromophore dynamics in the cavity of the cage, we estimated the possibility of phenyl ring rotation (φ-rotation, Figure 2) in Cl-BI, and consequently, the transformation from Cl-BI to Cl-BI*. We modeled the potential energy surfaces (PESs) by varying the $C_1{=}C_2{-}C_3{=}C_4$ dihedral angle in the Cl-BI molecule (Figure 2). The calculated energy barrier was found to be 34.2 kJ/mol, which is in line with previously reported data for HBI-related chromophores.[63,64]

Based on photophysical measurements, which demonstrated that Cl-BI@**9** (~19 Å pore aperture) and Cl-BI@**10** (~19 Å pore aperture) possess exactly the same emission maximum, 593 nm (λ_{ex} = 350 nm, Figure 1e), and aforementioned control experiments, it is plausible to suggest that changes in the photophysical response in comparison with that in the solid state could be associated with a different molecular conformation (Cl-BI*) promoted by the confined space of the pore. In natural systems such as fluorescent proteins, changes in emission profiles are also associated with the chromophore molecular conformation. For instance, similar emission switching associated with the difference in chromophore molecular conformations was previously reported for the photoactive yellow protein (PYP).[65] Another literature example demonstrating the same trend is 3-fluorotyrosyl-green fluorescent protein ((3-F)Tyr GFP, Figure 2),[66] in particular, structural analysis of the *meta*-halogenated chromophore revealed the presence of two conformers, which affected the photophysical response of the protein. Our studies support the abovementioned trend that emission profile changes can correlate with chromophore conformer formation.

To further elaborate on the fact that changes in the molecular conformations could result in a significant bathochromic shift

in the emission profile, we have performed theoretical analysis. In agreement with literature,[67–70] our time-dependent density-functional-theory calculations revealed that absorption/emission of the Cl-BI chromophore is associated with the electronic transitions between the ground and first excited singlet states, and the largest contributions come from the frontier molecular orbitals (Figure S39). According to previous reports,[71–73] BI-chromophores in tight (rigid) protein environments exhibit rather small Stokes shifts (~10 nm), while chromophores with large Stokes shifts (~50–70 nm) are surrounded by a much lower number of protein atoms.[72,73] This further agrees that within a rigid environment, the chromophore absorption and emission occur at an essentially fixed geometry associated with the ground electronic state. In other words, the tight confined space may not allow the chromophore molecule to change its geometry upon electronic excitation. Indeed, in our calculations for Cl-BI in the solid-state geometry, the lowest excitation is at 355 nm (Figure S42). Integration of the Cl-BI chromophore into larger pores (> 14 Å) could allow the molecule to change its geometry in the excited electronic state.

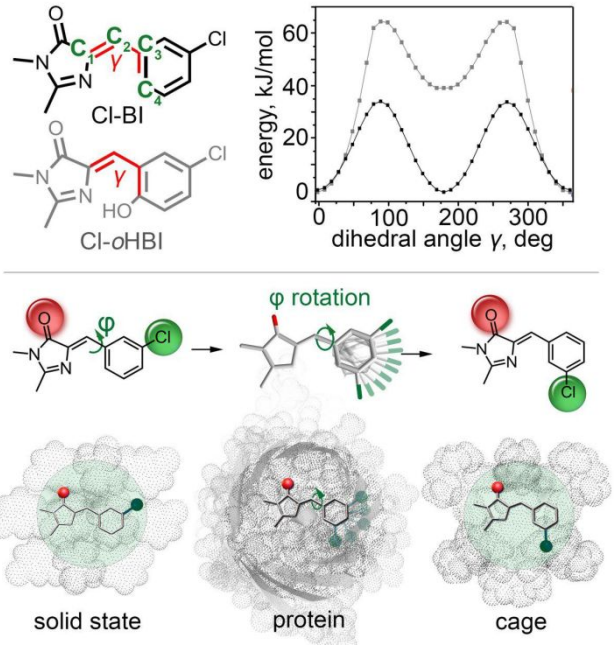

Figure 2. (*top, left*) Molecular structures of Cl-BI and Cl-*o*HBI chromophores. The dihedral angle (C_1=C_2–C_3=C_4, γ) used for potential energy surface (PES) modeling is shown in red. (*top, right*) PESs constructed for C_2–C_3 single bond dynamics in Cl-BI (black) and Cl-*o*HBI (gray). (*bottom*) A schematic representation of changes in molecular conformation of Cl-BI during chromophore incorporation inside a cage (Cl-BI*). The formation of different conformer occurs through φ-rotation around the C_2–C_3 single bond (green arrow). The red and green spheres emphasize the change in relative position of the oxygen atom and *meta*-substituent on the phenyl ring before and after chromophore incorporation inside a cage. The bottom section represents chromophore molecular conformations: (*left*) in the solid state, (*middle*) inside a (3-F)Tyr GFP,[66] and (*right*) inside a cage.

For the Cl-BI* conformer, crystallographically detected in **9** and relaxed towards equilibrium in the first excited singlet state, such dynamics noticeably shifts the emission profile by 84 nm (Figure S42). To explore the geometry relaxation pathway, the emission maxima of a Cl-BI molecule were calculated as a function of tilt (τ) and twist (φ) angles (Figure S40) for the chromophore in the excited state (Figure S41). We found that even small changes in the dihedral angle τ led to a bathochromic shift. Carrying out a hula twist (simultaneous twist and tilt) to the chromophore in the excited state, similar to that experimentally observed for BI-chromophores,[5,67] the theoretical maximum emission of the excited state conformer (479 nm, Figure S42) red-shifts by an additional 40 nm for a total shift of 124 nm. Notably, the tremendous shift of the emission maximum was found to be 150 nm for Cl-BI@**10**. Thus, combining theoretical, crystallographic data, and photophysical data, it is plausible to hypothesize that changes in photophysical properties of the Cl-BI chromophore is a result of the confinement character of its molecular environment, which could not only influence the ground state chromophore geometry, but also restrict its relaxation in the excited electronic state.

In order to further examine host-guest interactions, we propose that the presence of strong intramolecular bonds in the chromophore structure could also affect its photoluminescent properties. To test this hypothesis, we prepared the 5-(5-chloro-2-hydroxybenzylidene)-2,3-dimethyl-3,5-dihydro-4*H*-imidazol-4-one chromophore (Cl-*o*HBI).[47] The chosen chromophore structure possesses a hydroxyl group as a substituent on the phenyl ring (Figure 2), which promotes the formation of a seven-membered-ring through OH···N intramolecular hydrogen bonding and fosters the bathochromic shift of chromophore emission in comparison with a chromophore that is not decorated with a hydroxyl-group on the phenyl ring.[47] As expected, the estimated rotational barrier confirms that formation of an intramolecular hydrogen bond caused an increase in the energy barrier from 34.2 kJ/mol to 64.2 kJ/mol for Cl-BI and Cl-*o*HBI, respectively (Figure 2). Despite the enhanced activation barrier for the C_2–C_3 bond rotation, integration of Cl-*o*HBI inside the cage still resulted in formation of Cl-*o*HBI* with a distinct molecular conformation in comparison with Cl-*o*HBI observed in the solid state (Figure S20). Indeed, the crystallographic analysis revealed that in the Cl-*o*HBI* structure, the chlorine and oxygen atoms are pointing in opposite directions (Figure 3). As in the case of Cl-BI*, the confined environment of the cage dictates the changes in Cl-*o*HBI* molecular conformation despite the requirement of breaking very strong intramolecular interactions such as hydrogen bonding. The chromophore conformation modifications resulted in changes of chromophore photophysical properties. The Cl-*o*HBI@$Pd_6(TPT)_4$ emission maximum was found to be 607 nm in contrast to 627 nm observed for Cl-*o*HBI chromophore in the solid state (Figure S24). We speculated that the observed changes in chromophore photophysical behavior (a hypsochromic shift) are associated with the confined space of the cage and can be potentially explained by disruption of hydrogen bonding, i.e., a seven-membered-ring breaking, from which an excited-state intramolecular proton transfer can take place.[74] Interestingly, the chromophore isolated inside the cage, Cl-*o*HBI*, does not have any structural analogues among the *ortho*-hydroxy-derivatives of HBI-chromophores (X-*o*HBI), i.e., all reported chromophore structures of X-*o*HBI contain the OH···N hydrogen bond.

Confined environment of DNA: a cage as a shuttle for chromophore transportation. Integration of the chromophore inside the water-soluble cage (**9**) not only allowed us to employ X-ray crystallography to reveal the chromophore conformation but also provided a unique opportunity to investigate the effect of the confined space of DNA on a

photophysical response of the chromophore. As previously reported, DNA fosters control over chromophore geometry through a series of weak interactions, such as π-π stacking, hydrogen bonding, and/or van der Waals interactions.[75] Although there are a number of requirements including size, planarity, and ability to participate in hydrogen bonding, imposed on the chromophore molecule to promote successful chromophore-DNA interactions;[76,77] the Cl-*o*HBI chromophore satisfies the listed criteria. In this case, the chromophore-DNA interactions are limited due to the hydrophobic nature of Cl-*o*HBI chromophore but this challenge can be overcome through utilization of a water-soluble cage (**9**) as a chromophore carrier.

Prior to chromophore integration into the confined space of DNA, we explored the possibility of the cage to release the Cl-*o*HBI chromophore in aqueous media through photophysical studies (more details in the Supporting Information).

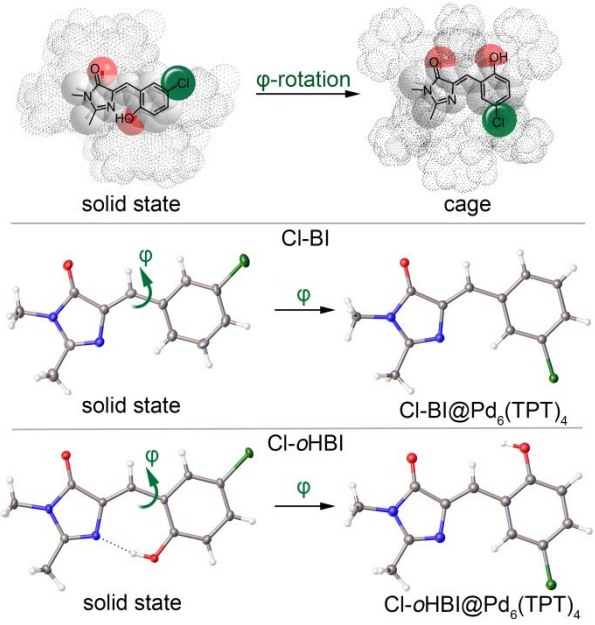

Figure 3. (*top*) A schematic representation of changes in the molecular conformation of Cl-*o*HBI during incorporation inside the $Pd_6(TPT)_4$ cage. The green and red spheres demonstrate the changes in relative positions of chlorine and oxygen atoms, respectively. (*middle and bottom*) Single-crystal X-ray structures of Cl-BI and Cl-*o*HBI in the solid state and incorporated inside the $Pd_6(TPT)_4$ cage. The corresponding changes are depicted by the green arrow. Thermal ellipsoids are shown at the 40% probability level. Blue, red, gray, green, and white spheres represent N, O, C, Cl, and H atoms, respectively.

As expected, Cl-*o*HBI release is accompanied by a decrease of Cl-*o*HBI@$Pd_6(TPT)_4$ emission intensity (λ_{max} = 625 nm; λ_{ex} = 300 nm), while the emission signal at 430 nm (λ_{ex} = 300 nm) corresponding to the empty cage increased (Figure S25). Moreover, the addition of the DNA aqueous solution to either Cl-*o*HBI chromophore or empty cage $Pd_6(TPT)_4$ solutions in water did not reveal any emission enhancement (Figure 4a). In contrast, after addition of aqueous DNA solution (10 mg/mL in water) to aqueous Cl-*o*HBI@$Pd_6(TPT)_4$ solution, intensity of the emission maximum at 625 nm increased (Figure 4a). In particular, the intensity of the Cl-*o*HBI@$Pd_6(TPT)_4$-DNA solution was almost 100 times higher than that of the Cl-*o*HBI solution (Figure 4a). Therefore, we hypothesized that such photoluminescent enhancement occurs due to inhibition of non-radiative decay pathways in the confined environment of DNA. The observed tendency is in line with recent literature studies which describe a similar enhancement of emission response observed for HBI-based chromophores encapsulated between nucleic acids of fluorogenic RNAs.[78,79] To shed light on the possible mechanism of interactions between Cl-*o*HBI and DNA, we performed several control experiments. Based

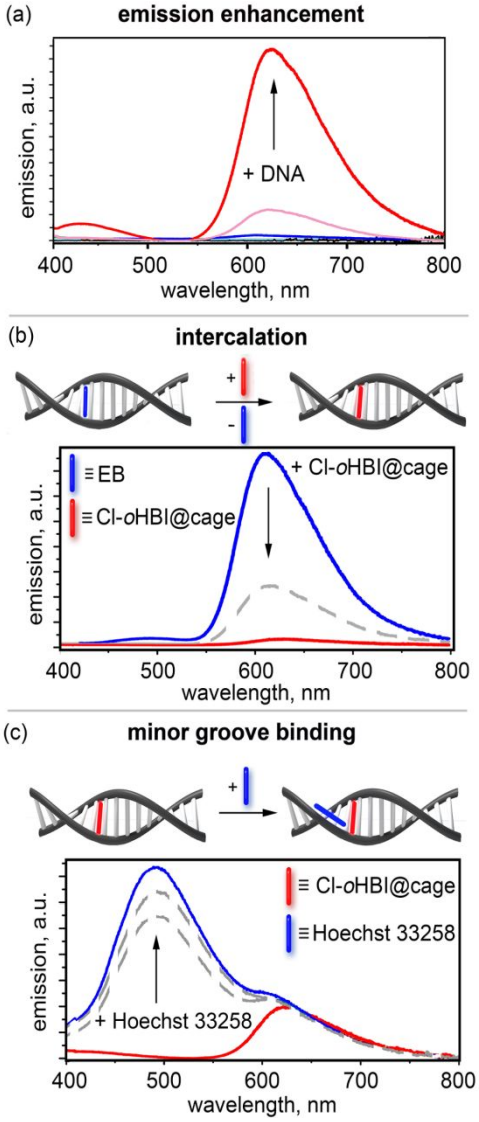

Figure 4. (*a*) Emission spectra of DNA (black), Cl-*o*HBI (light blue), Cl-*o*HBI-DNA (blue), Cl-*o*HBI@$Pd_6(TPT)_4$ (pink), and Cl-*o*HBI@$Pd_6(TPT)_4$-DNA (red). The black arrow shows the emission enhancement from pink to red spectra upon addition of DNA to Cl-*o*HBI@$Pd_6(TPT)_4$ aqueous solution. (*b*) A schematic representation of small molecules interaction with DNA through an intercalation mechanism. Blue and red rods represent ethidium bromide (EB) and Cl-*o*HBI chromophore, respectively. Fluorescence titration of EB with Cl-*o*HBI@$Pd_6(TPT)_4$ is shown. The black arrow shows a decrease of emission intensity upon an increase of Cl-*o*HBI@$Pd_6(TPT)_4$ concentration. (*c*) A schematic representation of small molecules interaction with DNA through a minor groove binding mechanism. Blue and red rods indicate Hoechst 33258 and Cl-*o*HBI@$Pd_6(TPT)_4$, respectively. Fluorescence titration of Cl-*o*HBI@$Pd_6(TPT)_4$ with Hoechst 33258 is shown. The black arrow shows the appearance of the emission maxima corresponding to the DNA-Hoechst 33258 complex. A 300 nm-excitation wavelength was used to acquire all fluorescence spectra.

on literature reports,[77] we hypothesized that initial interactions between Cl-*o*HBI@$Pd_6(TPT)_4$ and DNA were facilitated by electrostatic interactions between the positively charged cage and the partially negatively charged DNA.[77] Delving deeper, chromophore-DNA interactions could occur through two main mechanisms: intercalation or minor groove binding (Figure 4).[77] These mechanisms of guest-DNA interactions are usually probed by utilization of distinct dyes: ethidium bromide (EB, intercalation mechanism) and Hoechst 33258 (groove binding mechanism).[77] Therefore, we investigated the possible mechanism of interactions between Cl-*o*HBI and DNA by performing a competitive binding test between Cl-*o*HBI@$Pd_6(TPT)_4$ and dyes (EB or Hoechst 33258).

To probe the possibility of Cl-*o*HBI intercalation between two base pairs of DNA as shown in Figure 4b, we utilized photoluminescence spectroscopy and monitored changes in the emission response of an EB-DNA complex (590 nm)[80] by adding an aqueous solution of Cl-*o*HBI@$Pd_6(TPT)_4$. The increase of Cl-*o*HBI@$Pd_6(TPT)_4$ concentration in aqueous solution resulted in a decrease in the fluorescence intensity of the EB-DNA complex (Figure 4b), indicating that intercalated EB molecules were displaced by competing Cl-*o*HBI.

To address the possibility of minor groove binding, competitive studies between the Cl-*o*HBI-DNA complex and the Hoechst 33258 dye were also performed. The slow addition of Hoechst 33258 water solution to the Cl-*o*HBI-DNA complex did not result in the expected decrease in fluorescence intensity of the Cl-*o*HBI-DNA complex. Instead, it led to the appearance of an emission maxima at 510 nm, corresponding to the Hoechst 33258-DNA complex (Figure 4c).[81] Therefore, we suggest that the most plausible mechanism for Cl-*o*HBI interaction with DNA is based on intercalation of chromophore molecules between two base pairs of DNA. To summarize, these studies demonstrate the possibility to deliver the chromophore by using a cage in aqueous media and shed light on some mechanistic aspects of chromophore interactions promoted by the confined environment of DNA.

To further survey the idea of chromophore delivery to biological systems, we applied a similar approach as previously mentioned relative to testing the uptake and release of fluorescent Cl-*o*HBI from $Pd_6(TPT)_4$ to cells, specifically macrophages, with broad physiological functions. As shown in a number of literature reports,[82–84] attention towards bio-optical imaging is driven by the opportunity to image cellular activity of tagged biomolecules including proteins and nucleic acids (DNA/RNA) in real time. For instance, the development of novel fluorescent probes, emitting signal only after contact with specific target cells, are essential for dynamic visualization with direct applications in medical diagnostics and drug discovery.[85] Macrophages, which are phagocytic cells with essential roles in inflammation, immunity, and pathologies, were used to probe the possibility of uptake of such fluorescent probes. In particular, we investigated the uptake of Cl-*o*HBI by RAW264.7 macrophages using fluorescence microscopy.

For initial uptake screening, we incubated RAW264.7 macrophages in a water solution of Cl-*o*HBI@$Pd_6(TPT)_4$ at 37 °C (physiological temperature) for 4 h. The acquired fluorescent images showed that Cl-*o*HBI released from the cage and stained the cells with a visible fluorescence response (Figure 5). The performed control experiments which include incubation of RAW264.7 macrophages with water solutions of either Cl-*o*HBI or $Pd_6(TPT)_4$ did not show any fluorescence response under the same experimental and imaging conditions (Figure 5). Thus, our preliminary studies spur the application of a self-assembled coordination cage as a water-soluble cargo carrier for potential delivery of small fluorescent probes to biological objects with the possibility to extend such applications to real-time imaging in the future.

In addition to one-pot delivery of the chromophore to biological systems as shown above, a strategy of *in situ* chromophore formation has been reported. This approach was used to study the kinetics of intracellular processes on the example of GFP-related chromophore preparation directly inside the HeLa cells.[86]

In our work, we decided to probe the feasibility of *in situ* chromophore formation, i.e., carry out the reaction for chromophore formation in the confined space of a framework.

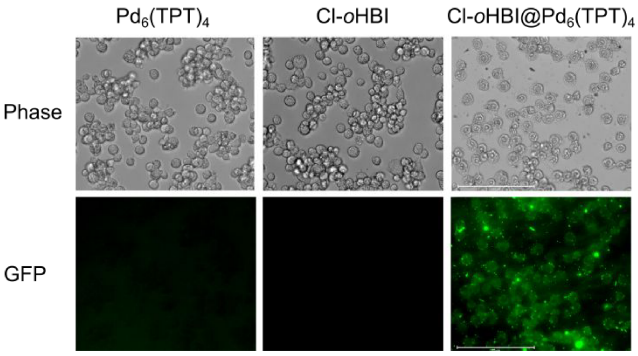

Figure 5. Fluorescence images of RAW 264.7 macrophage cells treated with water solutions of: (*left*) $Pd_6(TPT)_4$, (*middle*) Cl-*o*HBI, and (*right*) Cl-*o*HBI@$Pd_6(TPT)_4$. Scale bar represents 125 μm.

As a model system, we selected a framework that possesses: (i) sufficient pore size to accommodate reagents and resulting products; (ii) stability necessary to preserve structural integrity during reaction process; and (iii) an emission profile that does not interfere with the photophysical response of the incorporated chromophore. The covalent-organic scaffold **11** (Figure 6) made of 2,5-dimethoxyterephthalaldehyde and tri-(4-aminophenyl)benzene satisfies all of the mentioned criteria.[87] As a model reaction, we chose the formation of methyl 2-(4-(4-hydroxybenzylidene)-2-methyl-5-oxo-4,5-dihydro-1*H*-imidazol-1-yl)acetate (*p*OH-BI-CH_2COOCH_3) (Figure 6), which can be performed in one step by addition of methyl-2-((1-ethoxyethylidene)amino)acetate to an ethanol solution of 4-hydroxybenzaldehyde with a catalytic amount of acetic acid (Figure 6). Besides a facile synthetic route, this reaction could be considered as a model reaction for future bioimaging studies since hydroxybenzaldehydes are present in several cell cultures.[88]

We monitored the reaction progress inside **11** (Figure S38) through changes in the emission maximum of the reaction mixture (Figure 6). A gradual 70 nm bathochromic-shift in the emission profile was detected after the chromophore formation.[46,89] We envision that this concept may not only foreshadow the use of extended rigid frameworks and their confined environments for the development of fluorescent indicators, but also could open a new chapter in bioimaging, sensing, or designing materials with tunable emissive profiles.

Coordinatively immobilized chromophores inside a rigid scaffold. Up to this point in the manuscript, we focused on photophysics modulation and structure-photophysics

relationship of chromophores incorporated inside scaffolds as guest molecules. Our focus now turns to tethering and immobilizing a chromophore. A chromophore could potentially coordinate to any part of the MOF skeleton; however, all previous attempts at post-synthetic modifications or direct synthesis were exclusively focused on integration of the BI core as a part of the MOF linker[49,90,91] while, for instance, direct coordination of a HBI-based chromophore to a metal node is still a completely unexplored concept. In this work, we attempted to bridge this gap and study for the first time, the effect of short order interactions between a chromophore and the metal node of a MOF, as well as explore the subsequent influence on chromophore photophysics.

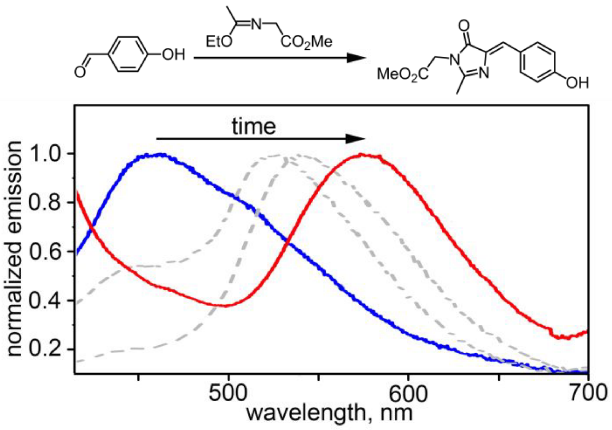

Figure 6. (*top*) Synthesis of *p*OH-BI-CH_2COOCH3. (*bottom*) Normalized emission spectra of starting (blue) and final reaction mixture inside the confined environment of **11** (red). Gray dashed lines represent the emission profile over time. An excitation wavelength of 350 nm was used to acquire all photoluminescence spectra of reaction mixture aliquots.

For this purpose, a novel chromophore, 4-((1-(carboxymethyl)-2-methyl-5-oxo-1,5-dihydro-4*H*-imidazol-4-ylidene)methyl)benzoic acid (*p*COOH-BI-CH_2COOH), was synthesized (Figure S26). This chromophore core was derivatized with carboxylate groups rendering it possible to coordinate to a metal node. As a scaffold for chromophore immobilization, we chose $Zr_6O_4(OH)_8(Me_2BPDC)_4$ ($Zr_6(Me_2BPDC)_4$) framework (Me_2BPDC^{2-} = 2,2′-dimethylbiphenyl-4,4′-dicarboxylate),[92] in which terminal –OH^-/H_2O groups on the metal nodes can be replaced by performing capping linker installation.[92] In addition, the emission profile of the chosen MOF does not interfere with the chromophore emission profile, allowing us to shift the focus of our studies to solely the metal node binding effect.

Post-synthetic immobilization of the *p*COOH-BI-CH_2COOH linker was achieved by heating the $Zr_6(Me_2BPDC)_4$ framework in a saturated DMF solution of *p*COOH-BI-CH_2COOH at 75 °C for 24 h and resulted in the formation of $Zr_6(Me_2BPDC)_4$(*p*COOH-BI-$CH_2COO)_2$ (Figure 7b). Chromophore binding to the metal node was confirmed by single-crystal X-ray analysis. Crystallographic studies also revealed that *p*COOH-BI-CH_2COO^- is covalently bound to the Zr-metal nodes and is oriented in a similar fashion to how the chromophore lies in a *β*-barrel cavity of a fluorescent protein, Clover (Figure 7a). Thus, these studies are the first example of HBI-chromophore coordination to a metal node as well as the first example of MOF immobilization of a HBI-chromophore through a derivatized imidazolone core, similarly to integration of HBI derivatives in natural proteins.[93]

As a result of coordinative immobilization of *p*COOH-BI-CH_2COO^- to the MOF, $Zr_6(Me_2BPDC)_4$(*p*COOH-BI-$CH_2COO)_2$ became emissive compared to the non-emissive parent framework (Figure 7c). The emission maximum of $Zr_6(Me_2BPDC)_4$(*p*COOH-BI-$CH_2COO)_2$ is 510 nm (λ_{ex} = 350 nm) and is hypsochromically-shifted compared to the 550-nm-centered emission (λ_{ex} = 350 nm) detected for the chromophore in the solid state (Figure 7c). Interestingly, the observed emission of $Zr_6(Me_2BPDC)_4$(*p*COOH-BI-$CH_2COO)_2$ falls in the range of emission maxima for natural proteins with a HBI core (Figure 7c). The structural analysis of different fluorescent proteins presented in the Protein Data Bank (PDB)[94] showed that there is one common chromophore, (*Z*)-2-(2-(aminomethyl)-4-(4-hydroxybenzylidene)-5-oxo-4,5-dihydro-1*H*-imidazol-1-yl)acetic acid (CR2), for more than 85 PDB entries of different fluorescent proteins. In all these structures, the HBI-based ligand is attached to the *α*-helix of a protein through the bond between the imidazolone ring and the amino acid residues.[93] In Figure 7d, emission maxima as a function of an excitation maximum for fluorescent proteins (with a unique CR2 ligand) and *p*COOH-BI-CH_2COOH chromophore bound to MOF metal node are shown. The presented approach could provide a model for mechanistic studies for development of novel protein mimics emissive in a wide spectral range.

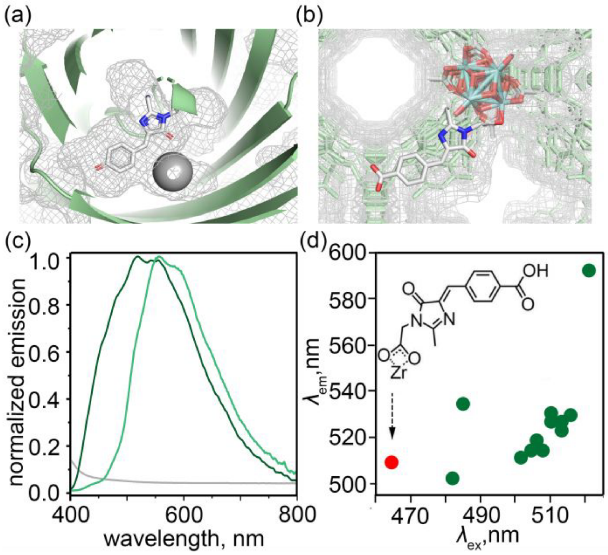

Figure 7. (*a*) A part of the X-ray crystal structure of a fluorescent protein, Clover, highlighting chromophore orientation inside the *β*-barrel cavity. (*b*) A part of the X-ray crystal structure of $Zr_6(Me_2BPDC)_4$(*p*COOH-BI-$CH_2COO)_2$ highlighting *p*COOH-BI-CH_2COOH anchoring to the Zr-based metal node. (*c*) Normalized emission spectra of $Zr_6(Me_2BPDC)_4$ (gray), *p*COOH-BI-CH_2COOH (light green), and $Zr_6(Me_2BPDC)_4$(*p*COOH-BI-$CH_2COO)_2$ (dark green). (*d*) Emission maxima of fluorescent proteins with the unique CR2 ligand as a function of an excitation maximum. The red dot represents the synthesized $Zr_6(Me_2BPDC)_4$(*p*COOH-BI-$CH_2COO)_2$ framework.

To further elucidate the results of "fastening" a HBI-chromophore to a metal node on photophysical profile, theoretical modeling was implemented. Our preliminary PES simulations for C_2–C_3 single bond dynamics (Figure S27) performed by density functional theory calculations showed that a chromophore coordinated to the metal node possessed a slightly higher energy barrier, 39.6 kJ/mol, in comparison with

34.8 kJ/mol found for the unconstrained chromophore (Figure S27). Therefore, coordinative immobilization of the chromophore to the metal node could potentially lead to additional suppression of non-radiative pathways attributed to the confined space of a framework, and therefore, result in changes in the emission profile. Interestingly, *p*COOH-BI-CH_2COO^- bound to the metal node is a new conformer and differs from *p*COOH-BI-CH_2COOH observed in the solid state relative to the carboxyl group adjacent to the imidazolone ring (Figure S27). One of the possible pathways for a C_6–N bond "flip" (i.e., single bond C_6–N rotation) should go through an energy barrier of 51.0 kJ/mol. However, there is an alternative route associated with a much lower energy barrier (20.1 kJ/mol). The latter pathway is possibly stabilized by a hydrogen bond between the carbonyl oxygen on the imidazolone ring and the carboxyl group adjacent to the imidazolone ring and is likely more favorable taking into account the energetics associated with the processes (Figure S27). We envision that further elaboration of the described approach of "fasten immobilization" achieved through covalent bond formation between a chromophore and a metal node could provide a platform for more detailed studies of metal-to-ligand charge transfer, ligand-to-metal charge transfer, and ligand-to-ligand charge transfer processes.

CONCLUSION

To summarize, these studies shed light on the unrevealed potential of a confined environment for tailoring photophysical properties of hierarchical extended materials. For instance, a concept in which a MOF was used as a variable while the guest molecule remains unchanged to achieve tunability of photophysical profiles, was explored for the first time. Prior studies exclusively focused on the approach in which different chromophores (guest = variable) were integrated inside a framework (MOF = constant) promoting changes in material photoluminescent properties.

Furthermore, we utilized a molecular cage as a truncated model for a MOF to provide the first mechanistic insights as to how a confined environment affects molecular reorganization and intramolecular hydrogen bonding using X-ray diffraction and theoretical calculations. We extended our studies beyond supramolecular assemblies or hierarchical materials by providing the first mechanistic insights on HBI-chromophore behavior inside the confined space of DNA.

The first attempts to use the metal nodes of a framework for suppression of non-radiative pathways were demonstrated; such a strategy provides a blueprint to discovering structural and photophysical similarities between the chromophore immobilized inside an artificial MOF matrix and natural proteins. To conclude, the presented studies not only illustrate mechanistic insights of chromophore photophysics in a confined space, but also provide general guidelines for precise tailoring of the photophysical response of solid-state photoluminescent materials.

EXPERIMENTAL SECTION

Materials. Zinc(II) nitrate hexahydrate (technical grade, Ward's Science), zirconium(IV) chloride (99.5%, Alfa Aesar), cesium fluoride (99%, Oakwood Chemical), silver nitrate (>99%, Sigma Aldrich), potassium hydroxide (ACS grade, Fisher Chemical), sodium hydroxide (ACS grade, Macron Fine Chemicals), lithium hydroxide monohydrate (99%, Oakwood Chemical), potassium carbonate (ACS grade, BDH), sodium nitrite (ACS grade, Fisher Scientific), sodium azide (reagent grade, Oakwood Chemical), palladium(II) chloride (>99%, Oakwood Chemical), bis(triphenylphosphine)palladium(II) dichloride (96%, Oakwood Chemical), palladium(II) acetate (>95%, Oxchem), palladium on carbon (10% on carbon, Alfa Aesar), ammonium formate (98%, Chem-Impex International Inc.), 3-chlorobenzaldehyde (95%, Oxchem), 5-chloro-2-hydroxybenzaldehyde (97%, Ark Pharm), 4-hydroxybenzaldehyde (99.8%, Chem-Impex International Inc.), 4-carboxybenzaldehyde (99%, Chem-Impex International Inc.), terephthalaldehyde (95%, Oxchem), 4,4′-dipyridyl (99.29%, Chem-Impex International Inc.), 2,6-naphthalene-dicarboxylic acid (>98%, TCI America), 2,5-dihydroxyterephthalic acid (98%, TCI America), 1,3,5-benzenetricarboxylic acid (98%, Alfa Aesar), 4,4′-biphenyldicarboxylic acid (97%, Oakwood Chemical), terephthalic acid (>99%, TCI America), benzoic acid (99%, BeanTown Chemical), 1,3,5-tribromobenzene (>95%, Matrix Scientific), glycine methyl ester hydrochloride (98%, Acros Organics), ethyl acetimidate hydrochloride (97%, Alfa Aesar), methylamine (33% weight in absolute ethanol, 99%, Sigma-Aldrich), 2,5-dibromoaniline (97%, Oakwood Chemical), 4-methoxycarbonyl phenylboronic acid (>97%, Boronic Molecular), 4-aminophenyl boronic ester (reagent grade, Oakwood Chemical), triphenylphosphine (99%, Sigma-Aldrich), *N,N,N′,N′*-tetramethylethylenediamine (99%, Oakwood Chemical), 2,4,6-tris(4-pyridyl)-1,3,5-triazine (>97%, TCI America), methyl 4-iodo-3-methylbenzoate (98%, BeanTown Chemical), 4,4,4′,4′,5,5,5′,5′-octamethyl-2,2′-bi-(1,3,2-dioxaborolane) (>98%, Ark Pharm), sonicated salmon sperm DNA (10 mg/mL) Agilent Technologies, #201190), macrophage cells RAW 264.7 (ATCC®), phosphate buffered saline tablet (Sigma-Aldrich), ethidium bromide solution (reagent grade, Bio-Rad), Hoechst 33258, pentahydrate (bis-benzimide) (reagent grade, Fisher Scientific), rhodamine 6G (99%, Acros Organics), acridine yellow (98%, Acros Organics), polyethylene glycol 400 (lab grade, Merck Millipore), glacial acetic acid (ACS grade, BDH), trifluoroacetic acid (99%, Sigma-Aldrich), hydrochloric acid (ACS grade, Fisher Scientific), ethanol (200 proof, Decon Laboratories, Inc.), tetrahydrofuran (ACS grade, Macron Fine Chemicals), methanol (ACS grade, Fisher Scientific), *N,N*-dimethylformamide (ACS grade, BDH), acetonitrile (ACS grade, Fisher Scientific), diethyl ether (ACS grade, J. T. Baker® Chemicals), dimethyl sulfoxide (ACS grade, Fisher Scientific), hexane (ACS grade, Macron Fine Chemicals), chloroform (ACS grade, Macron), Aliquat 336 (reagent grade, Beantown chemical), chloroform-*d* (99.8%, Cambridge Isotope Laboratories, Inc.), deuterium oxide (99.8%, Cambridge Isotope Laboratories, Inc.), and dimethyl sulfoxide-d_6 (99.9%, Cambridge Isotope Laboratories, Inc.) were used as received.

The compounds 5-(3-chlorobenzylidene)-2,3-dimethyl-3,5-dihydro-4*H*-imidazol-4-one (Cl-BI),[46] 5-(5-chloro-2-hydroxybenzylidene)-2,3-dimethyl-3,5-dihydro-4*H*-imidazol-4-one (Cl-*o*HBI),[47] 4-((1-(2-methoxy-2-oxoethyl)-2-methyl-5-oxo-1,5-dihydro-4*H*-imidazol-4-ylidene)methyl)benzoic acid (*p*COOH-BI-CH_2COOCH_3),[49] methyl-2-((1-ethoxyethylidene)amino)acetate,[89] $Zn_3(BTC)_2$ (BTC^{3-} = benzene-1,3,5-tricarboxylate),[50] $Zn_4O(BTB)_2$ (BTB^{3-} = benzene-1,3,5-tribenzoate),[51] $Zr_6(BTB)_4(BP)_3$ (BP = 4,4′-bipyridyl),[52] $Zr_6O_4(OH)_4(BDC)_6$ (BDC^{2-} = terephthalate),[53] $Zn_4O(NDC)_3$ (NDC^{2-} = naphthalene-2,6-dicarboxylate),[54] Zn_2(DOBDC) ($DOBDC^{2-}$ = 2,5-dihydroxyterephthalate),[55] $Zr_6O_4(OH)_4(BPDC)_6$ ($BPDC^{2-}$ = biphenyl-4,4′-dicarboxylate),[53] $Zr_6O_4(OH)_4(TPDC\text{-}NH_2)_6$ ($TPDC\text{-}NH_2^{2-}$ = 2′-amino-terphenyl-4,4′-dicarboxylate),[53] $Zr_6O_4(OH)_{10}(BTB)_2$,[56] $Pd_6(TPT)_4$ (TPT = 2,4,6-tri(pyridin-4-yl)-1,3,5-triazine),[95] $Zr_6O_4(OH)_8(Me_2BPDC)_4$ ($Zr_6(Me_2BPDC)_4$, Me_2BPDC^{2-} = 2,2′-dimethylbiphenyl-4,4′-dicarboxylate),[92] and **11**[87] were prepared according to the reported procedures.

General procedure for preparation of Cl-BI@MOF. Incorporation of Cl-BI inside MOFs was performed during solvothermal synthesis of the corresponding framework. Initially, metal salt, linkers, and acid were combined according to each reported literature procedure to prepare MOFs: ($Zn_3(BTC)_2$,[50] $Zn_4O(BTB)_2$,[51] $Zr_6(BTB)_4(BP)_3$,[52] $Zr_6O_4(OH)_4(BDC)_6$,[53] $Zn_4O(NDC)_3$,[54] Zn_2(DOBDC),[55] $Zr_6O_4(OH)_4(BPDC)_6$,[53] $Zr_6O_4(OH)_4(TPDC\text{-}NH_2)_6$,[53] and $Zr_6O_4(OH)_{10}(BTB)_2$)[56]. For example, to prepare $Zn_3(BTC)_2$,

$Zn(NO_3)_2 \cdot 6H_2O$ (0.074 g, 0.25 mmol) and H_3BTC (0.053 g, 0.25 mmol), were mixed in 10 mL of DMF. To each vial, 0.050 g of Cl-BI was added, and the resulting solutions underwent solvothermal treatment to prepare the corresponding frameworks. The obtained crystals were thoroughly washed with *N,N*-dimethylformamide (DMF) to remove residual chromophore molecules from MOF surface. To quantify the amount of incorporated chromophore, Cl-BI@MOF samples were sonicated in DMF to extract the chromophore from the pores. The amount of chromophore inclusion was quantified using calibration curves obtained from solutions with known concentrations by UV-vis spectroscopy. Loadings of the chromophores after incorporation in $Zn_3(BTC)_2$, $Zn_4O(BTB)_2$, $Zn_6(BTB)_4(BP)_3$, $Zr_6O_4(OH)_4(BDC)_6$, $Zn_4O(NDC)_3$, $Zn_2(DOBDC)$, $Zr_6O_4(OH)_4(BPDC)_6$, $Zr_6O_4(OH)_4(TPDC\text{-}NH_2)_6$, and $Zr_6O_4(OH)_{10}(BTB)_2$ were found to be 0.013, 0.015, 0.047, 0.019, 0.026, 0.021, 0.071, 0.0031, and 0.047 wt%, respectively. The PXRD patterns of the prepared Cl-BI@MOF materials, Cl-BI@$Zr_6O_4(OH)_4(BDC)_6$, Cl-BI@$Zr_6O_4(OH)_4(BPDC)_6$, Cl-BI@$Zr_6O_4(OH)_4(TPDC\text{-}NH_2)_6$, Cl-BI@$Zn_6(BTB)_4(BP)_3$, Cl-BI@$Zn_4O(BTB)_2$, Cl-BI@$Zn_3(BTC)_2$, Cl-BI@$Zr_6O_4(OH)_{10}(BTB)_2$, Cl-BI@$Zn_2(DOBDC)$, and Cl-BI@$Zn_4O(NDC)_3$ are shown in Figures S1–S9.

Solvent exchange procedure. To estimate the effect of incorporated solvent molecules on the emission profile of the prepared frameworks, we performed solvent exchange experiments. The prepared $Zr_6O_4(OH)_4(TPDC\text{-}NH_2)_6$ framework underwent solvent exchange procedures with three different solvents (ethanol, chloroform, and ethyl acetate). After synthesis, a powder of $Zr_6O_4(OH)_4(TPDC\text{-}NH_2)_6$ was thoroughly washed with DMF to remove any unreacted materials. After washing with DMF, the MOF was soaked in the corresponding solvent at room temperature for 72 h to displace any DMF with a different solvent. The solvent was refreshed twice a day over three days before photophysical characterization to ensure complete solvent exchange (Figure S10). Solvent exchange of $Zr_6O_4(OH)_4(TPDC\text{-}NH_2)_6$ did not result in changes in the framework emission profile. Thus, the observed changes in the photophysical response of Cl-BI@MOF systems cannot be attributed to emission from the host.

Preparation of dye@MOF. To test the effect of the framework on the emission profile of incorporated guest molecules, we performed photoluminescence measurements using different dye molecules with the known photophysical profiles which were encapsulated in $Zr_6O_4(OH)_4(TPDC\text{-}NH_2)_6$. Generally, the emission profile of dyes changes upon inclusion inside a porous framework replicates the dye emission in solution rather than in the solid state. Rhodamine 6G and acridine yellow have been chosen as model dyes due to their distinct difference in photophysical response in solution and in the solid state, thus allowing for monitoring of the encapsulation process. In a 1-dram vial, $Zr_6O_4(OH)_4(TPDC\text{-}NH_2)_6$ (5.0 mg, 0.14 μmol) was added to a DMF solution of one of the corresponding dyes (rhodamine 6G or acridine yellow, C = 14 μM, 1.0 mL,). After 72 h, the resulting powder was washed with DMF to remove excess dye from MOF surface before photoluminescence measurements were performed (Figures S11 and S12).

Photoluminescent studies of Cl-BI chromophore in solvents. To estimate the solvent effect, we performed photoluminescent studies of Cl-BI in different solvents such as polar protic (methanol), polar aprotic (DMF, dimethyl sulfoxide), and nonpolar (toluene, dichloromethane). Fluorescence spectra of the corresponding solutions of Cl-BI (C = 0.5 mM) were measured at an excitation wavelength of 390 nm (Figure S13). For instance, the emission maxima of Cl-BI in DMF solution is slightly blue shifted (Δ = 6 nm) compared to that in the solid state (443 nm, λ_{ex} = 350 nm, Figure 1e). Furthermore, there is very little variation in the emission profile of Cl-BI chromophore in different solvents; $\Delta\lambda_{solvent}$ = 17 nm as evidenced in Figure S13.

Fluorescent studies of Cl-BI in the presence of MOF linkers. To investigate the possibility of Cl-BI interacting with the MOF linkers, a comparison among emission profiles of Cl-BI chromophore, linker, a mixture of linkers, and chromophore in both solid state and DMF solution, and Cl-BI@MOF were performed. An excitation wavelength of 350 nm was used to acquire all photoluminescence spectra. Fluorescence spectra of Cl-BI (C = 0.5 mM), MOF linker (C = 0.5 mM), and a mixture containing C = 0.5 mM of Cl-BI and MOF linker in DMF solutions were measured. Interactions between Cl-BI and MOF linkers did not result in significant changes in emission profile (Figures S14–17).

Preparation of Cl-BI@$Pd_6(TPT)_4$ and Cl-*o*HBI@$Pd_6(TPT)_4$. In a 20 mL vial, $Pd_6(TPT)_4$ (50.0 mg, 16.8 μmol) and the Cl-BI or Cl-*o*HBI chromophore (20.0 mg) were suspended in 1.00 mL of D_2O. The resulting suspension was stirred at 80 °C for 20 h. After heating, the obtained suspension was filtered and allowed to evaporate at room temperature to produce crystals of Cl-BI@$Pd_6(TPT)_4$ and Cl-*o*HBI@$Pd_6(TPT)_4$, which were suitable for single-crystal X-ray diffraction. The detailed description of data collection and refinement details are given in the Supporting Information (SI) and Table S1 contains the crystallographic refinement data. To quantify the amount of incorporated chromophore, Cl-BI@$Pd_6(TPT)_4$ and Cl-*o*HBI@$Pd_6(TPT)_4$ samples were sonicated in dichloromethane to extract the chromophore from the pores. The amount of chromophore inclusion was quantified spectrophotometrically as 1.2 wt% for Cl-BI@$Pd_6(TPT)_4$ and 3.3 wt% Cl-*o*HBI@$Pd_6(TPT)_4$ using calibration curves obtained from solutions with known concentrations by UV-vis spectroscopy. FTIR spectra are shown in Figures S22 and S23, respectively.

Release of Cl-*o*HBI chromophore from the cage. The difference in emission maxima between Cl-*o*HBI@$Pd_6(TPT)_4$ and the cage itself allowed us to monitor the release process of the chromophore from the cage. In particular, the emission profile of a water solution of Cl-*o*HBI@$Pd_6(TPT)_4$ exhibits a maximum intensity at 625 nm (λ_{ex} = 300 nm), while an aqueous solution of $Pd_6(TPT)_4$ emits at 430 nm (λ_{ex} = 300 nm). The chromophore release process was monitored by changes in emission intensity after dissolution of Cl-*o*HBI@$Pd_6(TPT)_4$. Figure S25 shows that the emission intensity significantly decreases during the first hour after the solution was prepared. The change in emission intensity can be explained by the release of the insoluble chromophore from the cage and its precipitation from the water media. Based on this experiment, we established a timeline for chromophore release, which was applied to study the interactions with DNA as the next step.

Fluorescent studies of chromophore-DNA interactions. To investigate the possibility of DNA interactions with Cl-*o*HBI after its release from $Pd_6(TPT)_4$, a solution of double-stranded DNA (18 μL, Agilent Technologies Sonicated Salmon Sperm DNA, #201190) was added to a freshly prepared water solution of Cl-*o*HBI@$Pd_6(TPT)_4$ (C = 90.0 μM, 175 μL) at room temperature. Fluorescence spectra from the mixture containing Cl-*o*HBI@$Pd_6(TPT)_4$ and DNA were measured at an excitation wavelength of 300 nm in a 5 mm micro quartz fluorometer cell (Starna Cell, Inc.). The solution in the quartz cell was placed in the fluorometer and unperturbed during the course of the experiment (24 h) and spectra were collected every 2 h (Figure 4a). As shown in Figure 4a, the emission intensity of Cl-*o*HBI increased after the addition of DNA.

As a control experiment, interactions of DNA with Cl-*o*HBI solution (not inside of the cage) were studied. The concentration of Cl-*o*HBI solution was estimated to match the concentration of Cl-*o*HBI inside $Pd_6(TPT)_4$ in the initial experiment (C = 16.0 μM). To prepare Cl-*o*HBI solution, a concentrated stock solution of Cl-*o*HBI in DMSO (C = 4.00 mM) was diluted to 16.0 μM with water. The final solution of Cl-*o*HBI (C = 6.85 μM, 175 μL) was mixed with DNA (18 μL) and fluorescence spectra were collected over time in a similar way as described above (Figure 4a).

Competitive binding studies with DNA. Competitive binding studies were performed to study the possibility to replace ethidium bromide (EB) from the EB-DNA complex with Cl-*o*HBI. An EB-DNA complex was prepared by combining EB in water (C = 2.4 μM,

10 μL) and 18 μL of DNA in water (0.10 mL). The binding effect of Cl-*o*HBI released from $Pd_6(TPT)_4$ was studied by adding 2 μL of Cl-*o*HBI@$Pd_6(TPT)_4$ solution (C = 16 μM, 10 μL) successively to a solution of EB-DNA complex (total number of additions was 5). The total amount of added Cl-*o*HBI was calculated to be slightly higher than the total amount of EB with the assumption that all added EB molecules intercalated. The influence of the addition of Cl-*o*HBI@$Pd_6(TPT)_4$ to the EB-DNA complex solution was determined by recording fluorescence emission spectra after each addition (Figure 4b).

In addition, we performed competitive binding studies with Hoechst 33258 in order to address the possibility of chromophore minor-groove binding. To a prepared solution of Cl-*o*HBI@$Pd_6(TPT)_4$ in water (C = 90.0 μM, 175 μL) with DNA (C = 10 mg/mL, 18 μL), 2 μL of a solution of Hoechst 33258 in water (C = 2.35 μM) was added successively (total number of additions was 3). Changes in the emission profile caused by interaction of Hoechst 33258 with DNA were monitored after each addition (Figure 4c). As shown in Figure 4c, the addition of Hoechst 33258 solution does not change the emission intensity of Cl-*o*HBI-DNA; however, the appearance of a new emission band at 485 nm was observed, corresponding to emission of the Hoechst 33258-DNA complex. Subsequent addition of Hoechst 33258 resulted in a shift of emission maxima to 510 nm due to saturation of DNA with Hoechst 33258 and the appearance of free Hoechst 33258 dye molecules in solution.

Synthesis of 4-((1-(carboxymethyl)-2-methyl-5-oxo-1,5-dihydro-4*H*-imidazol-4-ylidene)methyl)benzoic acid ($C_{14}H_{12}N_2O_5$, *p*COOH-BI-CH_2COOH). A lithium hydroxide solution in water (C = 1.00 M, 662 μL) was added to a solution of *p*COOH-BI-CH_2COOCH_3[49] (0.100 g, 35.0 mmol) in 15.0 mL of methanol, and the resulting solution was stirred for 24 h at room temperature. A precipitate formed and was collected by filtration, then washed with water and cold methanol. After drying under vacuum overnight, *p*COOH-BI-CH_2COOH was isolated in 37% yield. ^{1}H NMR (DMSO-d_6, 300 MHz): δ = 2.34 (3H, s), 4.43 (2H, s), 7.08 (1H, s), 7.99 (2H, d, J = 8.63 Hz), 8.32 (2H, d, J = 8.50 Hz), and 13.20 (1H, s) ppm (Figure S28). ^{13}C NMR (DMSO-d_6, 101 MHz): δ = 15.79, 41.85, 124.32, 129.93, 131.83, 132.30, 138.45, 140.24, 165.49, 167.37, 169.89, and 169.91 ppm (Figure S28). FTIR (neat, cm^{-1}): 3467, 1704, 1681, 1646, 1616, 1565, 1554, 1442, 1416, 1394, 1367, 1320, 1286, 1253, 1215, 1179, 1144, 1126, 1112, 911, 816, 775, 708, 693, and 662 (Figure S29). HRMS (ESI, m/z) calculated for $C_{14}H_{12}N_2O_5$ $[M+H]^+$ 289.0819, found 289.0816. Single-crystal X-ray data for the *p*COOH-BI-CH_2COOH chromophore are shown in Table S2 and Figure S26.

Preparation of $Zr_6(Me_2BPDC)_4$(*p*COOH-BI-$CH_2COO)_2$. In order to merge *p*COOH-BI-CH_2COOH with a MOF, a linker installation procedure was performed. In a 1-dram vial, crystals of $Zr_6(Me_2BPDC)_4$ (15 mg, 8.0 μmol) were added to a DMF solution of *p*COOH-BI-CH_2COOH (C = 30 mM, 4.0 mL). The vial was heated at 75 °C for 24 h, then cooled to room temperature. The obtained crystals were collected by filtration and washed with an excess of DMF to remove any unreacted materials. PXRD studies were used to confirm preservation of framework integrity after linker installation (Figure S30). FTIR spectrum is shown in Figure S31. The obtained crystals were suitable for single-crystal X-ray analysis. The detailed description of data collection and refinement details are shown in Figure 7b and Table S2.

Digestion procedure for $Zr_6(Me_2BPDC)_4$(*p*COOH-BI-$CH_2COO)_2$. To study the composition of the prepared $Zr_6(Me_2BPDC)_4$(*p*COOH-BI-$CH_2COO)_2$ MOF by ^{1}H NMR spectroscopy, a solution of 500 μL of DMSO-d_6 and 3 μL of concentrated HCl was added to 5 mg of the material, followed by sonication until complete sample dissolution. The percentage of the installed linker was calculated based on linker ratios found in the ^{1}H NMR spectrum of the digested sample (Figure S32).

Synthesis of methyl 2-(4-(4-hydroxybenzylidene)-2-methyl-5-oxo-4,5-dihydro-1*H*-imidazol-1-yl)acetate ($C_{14}H_{14}N_2O_4$, *p*OH-BI-CH_2COOCH_3). Prepared methyl-2-((1-ethoxyethylidene)amino)acetate (0.68 g, 4.3 mmol) was added to 4-hydroxybenzaldehyde (0.50 g, 4.1 mmol) in 5.0 mL of ethanol and 2 μL of acetic acid. After the resulting mixture was stirred vigorously for 4 h at room temperature, 15 mL of water was added, and the solution was stirred for an additional hour. The obtained yellow powder was collected by filtration and washed with water and hexane. After drying under vacuum, *p*OH-BI-CH_2COOCH_3 (0.39 g, 1.4 mol) was isolated in 34% yield. ^{1}H NMR (DMSO-d_6, 300 MHz): δ = 2.29 (3H, s), 3.71 (3H, s), 4.51 (2H, s), 6.85 (2H, d, J = 8.73 Hz), 6.96 (1H, s), 8.10 (2H, d, J = 8.73 Hz) and 10.18 (1H, s) ppm (Figure S34). ^{13}C NMR (DMSO-d_6, 101 MHz): δ = 15.48, 41.53, 52.99, 116.26, 125.53, 127.13, 134.84, 135.78, 160.32, 161.54, 169.15, and 169.87 ppm (Figure S34). FTIR (neat, cm^{-1}): 2954, 1741, 1712, 1642, 1598, 1552, 1516, 1444, 1364, 1302, 1276, 1214, 1169, 1149, 1086, 984, 911, 894, 841, 811, 786, 765, and 716 (Figure S35). HRMS (ESI, m/z) calculated for $C_{14}H_{14}N_2O_4$ $[M+H]^+$ 275.1026, found 275.1025. Single-crystal X-ray data for *p*OH-BI-CH_2COOCH_3 are shown in Table S3 and Figure S33.

Synthesis of *p*OH-BI-CH_2COOCH_3 inside of 11. In a 20 mL vial, **11** (15 mg, 5.4 μmol) was soaked in ethanol solution (10 mL) of 4-hydroxybenzaldehyde (0.010 g, 0.82 mmol) for 1 h. Then methyl-2-((1-ethoxyethylidene)amino)acetate (0.83 g, 5.2 mol) and 2 μL of acetic acid was added to the solution to initiate the reaction. The reaction process was monitored by solution photoluminescence studies by taking aliquots of the reaction mixture after 1.5 and 2.5 h (Figure 6). After 4 h of stirring at room temperature, 10 mL of water was added to the resulting suspension, followed by the formation of a white precipitate. The resulting suspension was stirred vigorously for an additional 2 h at room temperature. The obtained powder was collected by filtration and washed with DMF to remove any chromophore molecules on the COF surface. PXRD studies were employed to check framework crystallinity after the reaction (Figure S37).

Chromophore Delivery to RAW264.7 macrophages. RAW264.7 macrophage cells were seeded onto a Lab-Tek™ II Chamber Slide™ System and incubated in 37 °C until 70 % confluency. The prepared RAW264.7 cells were treated with water solutions of Cl-*o*HBI@$Pd_6(TPT)_4$, Cl-*o*HBI, or $Pd_6(TPT)_4$ (C = 5 mg/mL) and incubated for 4 h, then the cells were rinsed with phosphate buffered saline (PBS) to remove any unbound molecules. Finally, fluorescent images were acquired using the EVOS™ M7000 Imaging System at 20× magnification.

Fluorescence Spectroscopy. Steady-state emission spectra were acquired on an Edinburgh FS5 fluorescence spectrometer equipped with a 150 W Continuous Wave Xenon Lamp source for excitation. Emission measurements on solid samples and suspensions were collected using the front-facing module. For solid samples, powders of the appropriate materials were placed inside of a 0.5 mm quartz sample holder. Emission measurements on solutions were collected in quartz cuvettes in the appropriate solvent.

Other Physical Measurements. FTIR spectra were obtained on a Perkin-Elmer Spectrum 100. NMR spectra were collected on Bruker Avance III-HD 300 and Bruker Avance III 400 MHz NMR spectrometers. ^{13}C and ^{1}H NMR spectra were referenced to natural abundance ^{13}C peaks and residual ^{1}H peaks of deuterated solvents, respectively. Powder X-ray diffraction patterns were recorded on a Rigaku Miniflex II diffractometer with accelerating voltage and current of 30 kV and 15 mA, respectively. Solution UV-vis spectra were obtained at room temperature in the appropriate solvent in micro quartz cuvettes on a Perkin Elmer Lambda 35 spectrophotometer.

Computational Details. The electronic structure calculations have been performed using density functional theory (DFT), specifically the B3LYP functional paired with the 6-31G* basis to generate potential energy surface (PES) and with 6-31+G* to obtain excited electronic states. For the latter, the Grimme's dispersion correction has been invoked and the electronic excitations analysis is based on the time-dependent density functional theory (TDDFT) with the

random phase approximation (RPA).[96] The electronic structure method has been selected after additional calculations, including the ground state geometry optimization at the MP2 level using 6-31G* and 6-311+G** bases, which have yielded marginal differences in geometry compared to the DFT results. Selected excited state calculations were performed using LRC-ωPBEh density functional and yielded electronic excitations at slightly higher energies (by about 0.2 eV or 7%), and larger dipole moments (by ~ 0.15 D or 3-7%). As shown previously,[97] the accuracy of the dipole moments is rather insensitive to the DFT, thus our analysis is based on the B3LYP density functional. All calculations were performed using Spartan16 and Q-chem 5.2 software.[98,99]

The PESs illustrate single bond dynamics of Cl-BI, Cl-*o*HBI, and the unbound and confined *p*COOH-BI-CH_2COOH chromophore inside of the engineered scaffold. To model chromophore behavior inside of the framework, oxygen atoms were fixed to mimic the rigidity imposed by the scaffold. PESs were constructed by varying the dihedral angles C_1=C_2–C_3=C_4 and C_5–C_6–N–C_7 as shown in Figures 2 and S27.

In relation to the current experiments, we have examined the optical transitions corresponding to the ground and first excited singlet states of the Cl-BI chromophore.[67–70] A diagram of the electronic transitions pathway, presented in Figure S39, is shown for the molecular model of the Cl-BI chromophore in the solid state; S_0 and S_1 refer to the structures optimized in the ground electronic state, and $S_0'$and S_1' refer to the geometry optimized in the first excited singlet state. Absorption is associated with the optical transition from $S_0 \rightarrow S_1$, with the largest contributions coming from the highest occupied natural transition orbital (HONTO) and lowest unoccupied natural transition orbital (LUNTO) of the ground state. Emission involves the $S_1' \rightarrow S_0'$ transition represented primarily by the LUNTO and HONTO of the first excited singlet state at the optimized geometry. According to the electronic structure calculations, the two conformers – experimentally determined in the solid state and in the cage – are essentially degenerate in energy (the conformer in the cage is lower by less than 1 kJ/mol as computed with the B3LYP-D3/6-31+G* and MP2/6-311+G** methods) and the two conformers are separated by a small barrier of 34.2 kJ/mol (Figure 2). The benzene and imidazolone rings of the two experimental conformers are nearly in-plane: the twist (C_1=C_2–C_3=C_4, φ)/ the tilt (N–C_1=C_2–C_3, τ) angles (Figure S40) are 0.6°/0.7° and 178.4°/–8.2° for the conformer in the solid state and in the cage, respectively, while their excitation energies ($S_0 \rightarrow S_1$ and $S_1' \rightarrow S_0'$ transitions) are quite similar – the excitation from the ground state is different by 4 nm and emission from the first excited singlet state by 15 nm as computed with the B3LYP-D3/6-31+G* method. We also note that the two Cl-BI conformers show significant differences in their dipole moments: 5.25 and 2.53 D for the ground state of the conformer in the solid state and in the molecular cage, respectively, and both slightly reduced (5.10 and 2.16 D) in respect to the excited state.

Using the structural data available for the Cl-BI chromophore in the solid state and in the cage, we argue that the observed shift in emission can be attributed to the cage cavity (confinement effect). During geometry relaxation of the first excited singlet state twisting and tilting occur e.g., the twist angles for chromophore in the solid state and in the cage are 4.7° and 8.8°, respectively. Based on the cage cavity size (18.5 Å), it can 'freely' accommodate the Cl-BI chromophore with a size of ~14.4 Å (10.4 Å + 2.2 Å, which is the sum of the cage cavity size and two typical O···H distances). In contrast, the chromophore in the solid state and in the cavity of the MOFs with a small aperture (e.g., **1** = 11.0 Å and **2** = 12.0 Å) do not allow 'free' rotation of the chromophore. Therefore, we speculate that MOFs with a smaller pore size do not allow changes in twist and tilt angles, i.e., the geometry during absorption/emission remains stationary and their emission is similar to the photophysical profile of the absorption ($S_1 \rightarrow S_0$). On the contrary, MOFs with larger pore apertures can allow for the relaxation of the first excited singlet state geometry and their emission can be red-shifted compared to the solid state emission ($S_1' \rightarrow S_0'$).

Analysis of the electronic excitations obtained with TDDFT/RPA method based on B3LYP-D3/6-31+G* excited state optimization, yielded a shift in emission ($S_1' \rightarrow S_0'$, 439 nm, Figure S42) of 84 nm, respectively, compared to the emission in the solid state ($S_1 \rightarrow S_0$, 355 nm, Figure S42). Calculations using B3LYP/6-31+G*, CAM-B3LYP-D3/6-31+G*, and LRC-ωPBEh/6-311+G** resulted in similar values of emission shift (82, 76, and 80 nm). Allowing for the hula twist (simultaneous twist and tilt) of the molecule in the excited state, similar to that experimentally observed for BI-chromophore,[5,67] the theoretical maximum in emission from the excited state conformer (479 nm, Figure S42) red-shifted by additional 40 nm for a total shift of 124 nm compared to chromophore in the solid state. The trend in computed emission profile is qualitatively similar to the experimental emission as shown in Figure 1e. Compared to the solid state, the nonrigid confined environment may allow additional tilting and twisting of the Cl-BI chromophore in the excited state. The optical transitions are sensitive to such changes in geometry as illustrated in the optical transition profiles in Figure S41. An increase in φ angle from 0° to 50° resulted in a hypsochromic shift of 18 nm for the emission maxima, while an increase in τ angle from 0° to 50° leads to a bathochromic shift of 94 nm for the emission (Figure S41).

ASSOCIATED CONTENT

The Supporting Information is available free of charge on the ACS Publications website.

X-ray structure refinement data of prepared MOFs, PXRD patterns, FTIR, ^{1}H and ^{13}C spectra, photoluminescence spectra (PDF)

Crystallographic information for Cl-BI@$Pd_6(TPT)_4$ CCDC 1895560(CIF)

Crystallographic information for Cl-*o*HBI@$Pd_6(TPT)_4$ CCDC 1895561 (CIF)

Crystallographic information for *p*COOH-BI-CH_2COOH, CCDC 1895562 (CIF)

Crystallographic information for $Zr_6(Me_2BPDC)_4$(*p*COOH-BI-$CH_2COO)_2$, CCDC 1895563 (CIF)

Crystallographic information for *p*OH-BI-CH_2COOCH_3, CCDC 1895564 (CIF)

AUTHOR INFORMATION

Corresponding Author

*shustova@sc.edu

ACKNOWLEDGMENT

N.B.S. gratefully acknowledges support from the NSF CAREER Award (DMR-1553634), the Dreyfus Teaching-Scholar Award supported by the Dreyfus foundation, the Sloan Research Fellowship provided by the Alfred P. Sloan foundation, and a Cottrell Scholar Award from the Research Corporation for Science Advancement. M.S.F. acknowledges CONICET and Fulbright fellowships.

REFERENCES

(1) Brown, J. W.; Henderson, B. L.; Kiesz, M. D.; Whalley, A. C.; Morris, W.; Grunder, S.; Deng, H. Furukawa, H.; Zink, J. I.; Stoddart, J. F.; Yaghi, O. M. Photophysical Pore Control in an Azobenzene-Containing Metal-Organic Framework. *Chem. Sci.* **2013**, *4*, 2858–2864.

(2) Cho, E. N.; Zhitomirsky, D.; Han, G. G. D.; Liu, Y.; Grossman, J. C. Molecularly Engineered Azobenzene Derivatives for High Energy Density Solid-State Solar Thermal Fuels. *ACS Appl. Mater. Interfaces* **2017**, *9*, 8679–8687.

(3) Morabito, J. V.; Chou, L.-Y.; Li, Z.; Manna, C. M.; Petroff, C. A.; Kyada, R. J.; Palomba, J. M.; Byers, J. A.; Tsung, C.-K. Molecular Encapsulation beyond the Aperture Size Limit through Dissociative Linker Exchange in Metal-Organic Framework Crystals. *J. Am. Chem. Soc.* **2014**, *136*, 12540–12543.

(4) Katsoulidis, A. P.; Antypov, D.; Whitehead, G. F. S.; Carrington, E. J.; Adams, D. J.; Berry, N. G.; Darling, G. R.; Dyer, M. S.; Rosseinsky, M. J. Chemical Control of Structure and Guest Uptake by a Conformationally Mobile Porous Material. *Nature* **2019**, *565*, 213–217.

(5) Chang, J.; Romei, M. G.; Boxer, S. G. Structural Evidence of Photoisomerization Pathways in Fluorescent Proteins. *J. Am. Chem. Soc.* **2019**, *141*, 15504–15508.

(6) Newsome, W. J.; Ayad, S.; Cordova, J.; Reinheimer, E. W.; Campiglia, A. D.; Harper, J. K.; Hanson, K.; Uribe-Romo, F. J. Solid State Multicolor Emission in Substitutional Solid Solutions of Metal-Organic Frameworks. *J. Am. Chem. Soc.* **2019**, *141*, 11298–11303.

(7) Wang, L.; Moore, C. E.; Cohen, S. M. Coordinative Alignment To Achieve Ordered Guest Molecules in a Versatile Molecular Crystalline Sponge. *Cryst. Growth Des.* **2017**, *17*, 6174–6177.

(8) Pattengale, B.; Huang, J. Photoinduced Interfacial Charge Separation Dynamics in Zeolitic Imidazolate Framework. *Phys. Chem. Chem. Phys.* **2018**, *20*, 14884–14888.

(9) Tian, S.; Xu, S.; Liu, J.; He, C.; Xiong, Y.; Feng, P. Highly Efficient Removal of both Cationic and Anionic Dyes from Wastewater with a Water-Stable and Eco-Friendly Fe-MOF via Host-Guest Encapsulation. *J. Clean. Prod.* **2019**, *239*, 117767.

(10) Jiang, X.; Rodríguez-Molina, B.; Nazarian, N.; Garcia-Garibay, M. A. Rotation of a Bulky Triptycene in the Solid State: Toward Engineered Nanoscale Artificial Molecular Machines. *J. Am. Chem. Soc.* **2014**, *136*, 8871–8874.

(11) Larsen, R. W.; Wojtas, L. Photophysical Properties of $[Ru(2,2'\text{-bipyridine})_3]^{2+}$ Encapsulated Within the UiO-66 Zirconium Based Metal Organic Framework. *J. Solid State Chem.* **2017**, *247,* 77–82.

(12) Zharov, I.; Khabibullin, A. Surface-Modified Silica Colloidal Crystals: Nanoporous Films and Membranes with Controlled Ionic and Molecular Transport. *Acc. Chem. Res.* **2014**, *47*, 440–449.

(13) Sava Gallis, D. F.; Rohwer, L. E. S.; Rodriguez, M. A.; Nenoff, T. M. Efficient Photoluminescence via Metal-Ligand Alteration in a New MOFs Family. *Chem. Mater.* **2014**, *26*, 2943–2951.

(14) Jensen, S.; Tan, K.; Lustig, W.; Kilin, D.; Li, J.; Chabal, Y. J.; Thonhauser, T. Quenching of Photoluminescence in a Zn-MOF Sensor by Nitroaromatic Molecules. *J. Mater. Chem. C,* **2019**, *7*, 2625–2632.

(15) Zhang, Y.; Yuan, S.; Day, G.; Wang, X.; Yang, X.; Zhou, H.-C. Luminescent Sensors Based on Metal-Organic Frameworks. *Coord. Chem. Rev.* **2018**, *354*, 28–45.

(16) Kreno, L. E.; Leong, K.; Farha, O. K.; Allendorf, M.; Van Duyne, R. P.; Hupp, J. T. Metal-Organic Framework Materials as Chemical Sensors. *Chem. Rev.* **2012**, *112*, 1105–1125.

(17) Mallick, A.; Purkayastha, P.; Chattopadhyay, N. Photoprocesses of Excited Molecules in Confined Liquid Environments: An Overview. *J Photochem. Photobiol.* C **2007**, *8*, 109–127.

(18) Xue, M.; Zink, J. I. Probing the Microenvironment in the Confined Pores of Mesoporous Silica Nanoparticles. *J. Phys. Chem. Lett.* **2014**, *5*, 839−842.

(19) Maza, W. A.; Morris, A. J. Photophysical Characterization of a Ruthenium(II) Tris(2,2′-bipyridine)-Doped Zirconium UiO-67 Metal-Organic Framework. *J. Phys. Chem. C* **2014**, *118*, 8803−8817.

(20) Lin, J.; Hu, D.-D.; Zhang, Q.; Li, D.-S.; Wu, T.; Bu, X.; Feng, P. Improving Photoluminescence Emission Efficiency of Nanocluster-Based Materials by In Situ Doping Synthetic Strategy. *J. Phys. Chem. C* **2016**, *120*, 29390–29396.

(21) Wang, C.; Volotskova, O.; Lu, K.; Ahmad, M.; Sun, C.; Xing, L.; Lin, W. Synergistic Assembly of Heavy Metal Clusters and Luminescent Organic Bridging Ligands in Metal-Organic Frameworks for Highly Efficient X-ray Scintillation. *J. Am. Chem. Soc.* **2014**, *136*, 6171–6174.

(22) Choi, J. R.; Tachikawa, T.; Fujitsuka, M.; Majima, T. Evaluating Host-Guest Interactions in a Metal-Organic Framework Using a Polarity-Sensitive Probe. *J. Phys. Chem. Lett.* **2010**, *1*, 1101–1106.

(23) Zhao, B.; Li, N.; Wang, X.; Chang, Z.; Bu, X.-H. Host-Guest Engineering of Coordination Polymers for Highly Tunable Luminophores Based on Charge Transfer Emissions. *ACS Appl. Mater. Interfaces* **2017**, *9*, 2662–2668.

(24) Fei, Z.; Kocher, N.; Mohrschladt, C. J.; Ihmels, H.; Stalke, D. Single Crystals of the Disubstituted Anthracene 9,10-$(Ph_2P{=}S)_2C_{14}H_8$ Selectively and Reversibly Detect Toluene by Solid-State Fluorescence Emission. *Angew. Chem. Int. Ed.* **2003**, *42*, 783–787.

(25) Wu, X.-H.; Luo, P.; Wei, Z.; Li, Y.-Y.; Huang, R.-W.; Dong, X.-Y.; Li, K.; Zang, S.-Q.; Tang, B. Z. Guest-Triggered Aggregation-Induced Emission in Silver Chalcogenolate Cluster Metal-Organic Frameworks. *Adv. Sci.* **2019**, *6*, 1801304.

(26) Dolgopolova, E. A.; Rice, A. M.; Martin, C. R.; Shustova, N. B. Photochemistry and Photophysics of MOFs: Steps Towards MOF-Based Sensing Enhancements. *Chem. Soc. Rev.* **2018**, *47*, 4710–4728.

(27) Williams, D. E.; Shustova, N. B. Metal-Organic Frameworks as a Versatile Tool To Study and Model Energy Transfer Processes. *Chem. Eur. J.* **2015**, *21*, 15474–15479.

(28) Yu, J.; Li, X.; Deria, P. Light-Harvesting in Porous Crystalline Compositions: Where We Stand toward Robust Metal-Organic Frameworks. *ACS Sustainable Chem. Eng.* **2019**, *7*, 1841–1854.

(29) Stavila, V.; Talin, A. A.; Allendorf, M. D. MOF-Based Electronic and Opto-Electronic Devices. *Chem. Soc. Rev.* **2014**, *43*, 5994–6010.

(30) Zhang, T.; Lin, W. Metal-Organic Frameworks for Artificial Photosynthesis and Photocatalysis. *Chem. Soc. Rev.* **2014**, *43*, 5982–5993.

(31) So, M. C.; Wiederrecht, G. P.; Mondloch, J. E.; Hupp, J. T.; Farha, O. K. Metal-Organic Framework Materials for Light-Harvesting and Energy Transfer. *Chem. Commun.* **2015**, *51*, 3501–3510.

(32) Liu, J.; Zhuang, Y.; Wang, L.; Zhou, T.; Hirosaki, N.; Xie, R.-J. Achieving Multicolor Long-Lived Luminescence in Dye-Encapsulated Metal-Organic Frameworks and Its Application to Anticounterfeiting Stamps. *ACS Appl. Mater. Interfaces* **2018**, *10*, 1802–1809.

(33) Ye, Y.; Zhao, L.; Hu, S.; Liang, A.; Li, Y.; Zhuang, Q.; Tao, G.; Gu, J. Specific Detection of Hypochlorite Based on the Size-Selective Effect of Luminophore Integrated MOF-801 Synthesized by a One-Pot Strategy. *Dalton Trans.* **2019**, *48*, 2617–2625.

(34) Han, T. T.; Bai, H. L.; Liu, Y. Y.; Ma, J. F. Two Host-Guest Hybrids by Encapsulation AlQ_3 in Zeolitic Imidazolate Framework-8 as Luminescent Sensors for Fe^{3+}, CrO_4^{2-} and Acetone. *J. Solid State Chem.* **2019**, *269*, 588–593.

(35) Chen, R.; Zhang, J.; Chelora, J.; Xiong, Y.; Kershaw, S. V.; Li, K. F.; Lo, P.-K.; Cheah, K. W.; Rogach, A. L.; Zapien, J. A.; Lee, C.-S. Ruthenium(II) Complex Incorporated UiO-67 Metal-Organic Framework Nanoparticles for Enhanced Two-Photon Fluorescence Imaging and Photodynamic Cancer Therapy. *ACS Appl. Mater. Interfaces* **2017**, *9*, 5699–5708.

(36) Mieno, H.; Kabe, R.; Notsuka, N.; Allendorf, M. D.; Adachi, C. Long-Lived Room-Temperature Phosphorescence of Coronene in Zeolitic Imidazolate Framework ZIF-8. *Adv. Optical Mater.* **2016**, *4*, 1015–1021.

(37) Yoo, J.; Ryu, U.; Kwon, W.; Choi, K. M. A Multi-Dye Containing MOF for the Ratiometric Detection and Simultaneous Removal of $Cr_2O_7^{2-}$ in the Presence of Interfering Ions. *Sens. Actuator B Chem.* **2019**, *283*, 426–433.

(38) Zhao, X.; Wang, Y.; Hao, X.; Liu, W. Fluorescent Molecule Incorporated Metal-Organic Framework for Fluoride Sensing in Aqueous Solution. *Appl. Surf. Sci.* **2017**, *402*, 129–135.

(39) Glembockyte, V.; Frenette, M.; Mottillo, C.; Durantini, A. M.; Gostick, J.; Štrukil, V.; Friščić, T.; Cosa, G. Highly Photostable

and Fluorescent Microporous Solids Prepared via Solid-State Entrapment of Boron Dipyrromethene Dyes in a Nascent Metal-Organic Framework. *J. Am. Chem. Soc.* **2018**, *140*, 16882–16887.

(40) Ryu, U.; Yoo, J.; Kwon, W.; Choi, K. M. Tailoring Nanocrystalline Metal-Organic Frameworks as Fluorescent Dye Carriers for Bioimaging. *Inorg. Chem.* **2017**, *56*, 12859–12865.

(41) Liu, X.-Y.; Zhang, F.; Goh, T.-W.; Li, Y.; Shao, Y.-C.; Luo, L.; Huang, W.; Long, Y.-T.; Chou, L.-Y.; Tsung, C.-K. Using a Multi-Shelled Hollow Metal-Organic Framework as a Host to Switch the Guest-to-Host and Guest-to-Guest Interactions. *Angew. Chem. Int. Ed.* **2018**, *57*, 2110–2114.

(42) Huang, C.; Ye, Y.; Zhao, L.; Li, Y.; Gu, J. One-Pot Trapping Luminescent Rhodamine 110 into the Cage of MOF-801 for Nitrite Detection in Aqueous Solution. *J. Inorg. Organomet. Polym.* **2019**, *29*, 1476–1484.

(43) Zhou, Y.; Zhang, D.; Zeng, J.; Gan, N.; Cuan, J. A Luminescent Lanthanide-Free MOF Nanohybrid for Highly Sensitive Ratiometric Temperature Sensing in Physiological Range. *Talanta* **2018**, *181*, 410–415.

(44) Furukawa, H.; Cordova, K. E.; O'Keeffe, M.; Yaghi, O. M. The Chemistry and Applications of Metal-Organic Frameworks. *Science* **2013**, *341*, 1230444.

(45) Zhou, H.-C.; Long, J. R.; Yaghi, O. M. Introduction to Metal-Organic Frameworks. *Chem. Rev.* **2012**, *112*, 673–674.

(46) Baldridge, A.; Kowalik, J.; Tolbert, L. M. Efficient Synthesis of New 4-arylideneimidazolin-5-ones Related to the GFP Chromophore by 2+3 Cyclocondensation of Arylideneimines with Imidate Ylides. *Synthesis.* **2010**, *14*, 2424–2436.

(47) Dolgopolova, E. A.; Rice, A. M.; Smith, M. D.; Shustova, N. B. Photophysics, Dynamics, and Energy Transfer in Rigid Mimics of GFP-Based Systems. *Inorg. Chem.* **2016**, *55*, 7257–7264.

(48) Cui, Y.; Song, T.; Yu, J.; Yang, Y.; Wang, Z.; Qian, G. Dye Encapsulated Metal-Organic Framework for Warm-White LED with High Color-Rendering Index. *Adv. Funct. Mater.* **2015**, *25*, 4796–4802.

(49) Dolgopolova, E. A.; Moore, T. M.; Ejegbavwo, O. A.; Pellechia, P. J.; Smith, M. D.; Shustova, N. B. A Metal-Organic Framework as a Flask: Photophysics of Confined Chromophores with a Benzylidene Imidazolinone Core. *Chem. Commun.,* **2017**, *53*, 7361–7364.

(50) Song, X.; Jeong, S.; Kim, D.; Lah, M. S. Transmetalations in Two Metal-Organic Frameworks with Different Framework Flexibilities: Kinetics and Core-Shell Heterostructure. *CrystEngComm,* **2012**, *14*, 5753–5756.

(51) Leong, K.; Foster, M. E.; Wong, B. M.; Spoerke, E. D.; Van Gough, D.; Deaton, J. C.; Allendorf, M. D. Energy and Charge Transfer by Donor–Acceptor Pairs Confined in a Metal-Organic Framework: a Spectroscopic and Computational Investigation. *J. Mater. Chem. A,* **2014**, *2*, 3389–3398.

(52) Song, X.; Kim, T. K.; Kim, H.; Kim, D.; Jeong, S.; Moon, H. R.; Lah, M. S. Post-Synthetic Modifications of Framework Metal Ions in Isostructural Metal-Organic Frameworks: Core-Shell Heterostructures via Selective Transmetalations. *Chem. Mater.* **2012**, *24*, 3065–3073.

(53) Schaate, A.; Roy, P.; Godt, A.; Lippke, J.; Waltz, F.; Wiebcke, M.; Behrens, P. Modulated Synthesis of Zr-Based Metal-Organic Frameworks: From Nano to Single Crystals. *Chem. Eur. J.* **2011**, *17*, 6643–6651.

(54) Eddaoudi, M.; Kim, J.; Vodak, D.; Sudik, A.; Wachter, J.; O'Keeffe, M.; Yaghi, O. M. Geometric Requirements and Examples of Important Structures in the Assembly of Square Building Blocks. *Proc. Natl. Acad. Sci.* **2002**, *99*, 4900–4904.

(55) Rosi, N. L.; Kim, J.; Eddaoudi, M.; Chen, B.; O'Keeffe, M.; Yaghi, O. M. Rod Packings and Metal-Organic Frameworks Constructed from Rod-Shaped Secondary Building Units. *J. Am. Chem. Soc.* **2005**, *127*, 1504–1518.

(56) Wang, R.; Wang, Z.; Xu, Y.; Dai, F.; Zhang, L.; Sun, D. Porous Zirconium Metal-Organic Framework Constructed from 2D → 3D Interpenetration Based on a 3,6-Connected kgd Net. *Inorg. Chem.* **2014**, *53*, 7086–7088.

(57) Inokuma, Y.; Kawano, M.; Fujita, M. Crystalline Molecular Flasks. *Nat. Chem.* **2011**, 3, 349–358.

(58) Walton, I. M.; Cox, J. M.; Coppin, J. A.; Linderman, C. M.; Patel, D. G. (D.); Benedict, J. B. Photo-Responsive MOFs: Light-Induced Switching of Porous Single Crystals Containing a Photochromic Diarylethene. *Chem. Commun.* **2013**, *49*, 8012–8014.

(59) Sapchenko, S. A.; Samsonenko, D. G.; Dybtsev, D. N.; Melgunov, M. S.; Fedin, V. P. Microporous Sensor: Gas Sorption, Guest Exchange and Guest-Dependant Luminescence of Metal–Organic Framework. *Dalt. Trans.* **2011**, *40*, 2196–2203.

(60) Kawano, M.; Fujita, M. Direct Observation of Crystalline-State Guest Exchange in Coordination Networks. *Coord. Chem. Rev.* **2007**, *251*, 2592–2605.

(61) Kawamichi, T.; Haneda, T.; Kawano, M.; Fujita, M. X-Ray Observation of a Transient Hemiaminal Trapped in a Porous Network. *Nature* **2009**, *461*, 633–635.

(62) Liu, Q.-K.; Ma, J.-P.; Dong, Y.-B. Highly Efficient Iodine Species Enriching and Guest-Driven Tunable Luminescent Properties Based on a Cadmium(II)-Triazole MOF. *Chem. Commun.* **2011**, *47*, 7185–7187.

(63) Baldridge, A.; Samanta, S. R.; Jayaraj, N.; Ramamurthy, V.; Tolbert, L. M. Steric and Electronic Effects in Capsule-Confined Green Fluorescent Protein Chromophores. *J. Am. Chem. Soc.* **2011**, *133*, 712–715.

(64) Samanta, S. R.; Da Silva, J. P.; Baldridge, A.; Tolbert, L. M.; Ramamurthy, V. A Latent Reaction in a Model GFP Chromophore Revealed upon Confinement: Photohydroxylation of *ortho*-Halo Benzylidene-3-Methylimidazolidiones via an Electrocylization Process. *Org. Lett.* **2014**, *16*, 3304–3307.

(65) Schotte, F.; Cho, H. S.; Kaila, V. R. I.; Kamikubo, H.; Dashdorj, N.; Henry, E. R.; Graber, T. J.; Henning, R.; Wulff, M.; Hummer, G.; Kataoka, M.; Anifinrud, P. A. Watching a Signaling Protein Function in Real Time via 100-ps Time-Resolved Laue Crystallography. *Proc. Natl. Acad. Sci.* **2012**, *109*, 19256–19261.

(66) Bae, J. H.; Pal, P. P.; Moroder, L.; Huber, R.; Budisa, N. Crystallographic Evidence for Isomeric Chromophores in 3-Fluorotyrosyl-Green Fluorescent Protein. *ChemBioChem* **2004**, *5*, 720–722.

(67) Usman, A.; Mohammed, O. F.; Nibbering, E. T. J.; Dong, J.; Solntsev, K. M.; Tolbert, L. M. Excited-State Structure Determination of the Green Fluorescent Protein Chromophore. *J. Am. Chem. Soc.* **2005**, *127*, 11214–11215.

(68) Weber, W.; Helm, V.; McCammon, J. A.; Langhoff, P. W. Shedding Light on the Dark and Weakly Fluorescent States of Green Fluorescent Proteins. *Proc. Natl. Acad. Sci. US.A* **1999**, *96*, 6177–6182.

(69) Timerghazin, Q. K.; Carlson, H. J.; Liang, C.; Campbell, R. E.; Brown, A. Computational Prediction of Absorbance Maxima for a Structurally Diverse Series of Engineered Green Fluorescent Protein Chromophores. *J. Phys. Chem. B* **2008**, *112*, 2533–2541.

(70) Ansbacher, T.; Srivastava, H. K.; Stein, T.; Baer, R.; Merkx, M.; Shurki, A. Calculation of Transition Dipole Moment in Fluorescent Proteins – Towards Efficient Energy Transfer. *Phys. Chem. Chem. Phys.* **2012**, *14*, 4109–4117.

(71) Pakhomov, A. A.; Martynov, V. I. GFP Family: Structural Insights into Spectral Tuning. *Chem. Biol.* **2008**, *15*, 755–764.

(72) Wachter, R. M.; Elsliger, M.-A.; Kallio, K.; Hanson, G. T.; Remington, S. J. Structural Basis of Spectral Shifts in the Yellow-Emission Variants of Green Fluorescent Protein. *Structure* **1998**, *6*, 1267–1277.

(73) Piatkevich, K. D.; Malashkevich, V. N.; Morozova, K. S.; Nemkovich, N. A.; Almo, S. C.; Verkhusha, V. V. Extended Stokes Shift in Fluorescent Proteins: Chromophore–Protein Interactions in a Near-Infrared TagRFP675 Variant. *Sci. Rep.* **2013**, *3*, 1847.

(74) Chuang, W.-T.; Hsieh, C.-C.; Lai, C.-H.; Lai, C.-H.; Shih, C.-W.; Chen, K.-Y.; Hung, W.-Y.; Hsu, Y.-H.; Chou, P.-T. Excited-State Intramolecular Proton Transfer Molecules Bearing *o*-Hydroxy Analogues of Green Fluorescent Protein Chromophore. *J. Org. Chem.* **2011**, *76*, 8189–8202.

(75) Pyle, A. M.; Rehmann, J. P.; Meshoyrer, R.; Kumar, C. V.; Turro, N. J.; Barton, J. K. Mixed-Ligand Complexes of Ruthenium(II): Factors Governing Binding to DNA. *J. Am. Chem. Soc.* **1989**, *111*, 3051–3058.

(76) Majouga, A. G.; Udina, A. V.; Beloglazkina, E. K.; Skvortsov, D. A.; Zvereva, M. I.; Dontsova, O. A.; Zyk, N. V.; Zefirov, N. S. Novel DNA Fluorescence Probes based on 2-Thioxo-Tetrahydro-4*H*-Imidazol-4-Ones: Synthetic and Biological Studies. *Tetrahedron Lett.* **2012**, *53*, 51–53.

(77) Ihmels, H.; Otto, D. Intercalation of Organic Dye Molecules into Double-Stranded DNA -- General Principles and Recent Developments. In *Supermolecular Dye Chemistry*; Würthner, F., Ed.; Springer-Verlag: Berlin/Heidelberg, **2005**, 161–204.

(78) Dou, J.; Vorobieva, A. A.; Sheffler, W.; Doyle, L. A.; Park, H.; Bick, M. J.; Mao, B.; Foight, G. W.; Lee, M. Y.; Gagnon, L. A.; Carter, L.; Sankaran, B.; Ovchinnikov, S.; Marcos, E.; Huang, P.-S.; Vaughan, J. C.; Stoddard, B. L.; Baker, D. De Novo Design of a Fluorescence-Activating *β*-Barrel. *Nature* **2018**, *561*, 485–491.

(79) Warner, K. D.; Chen, M. C.; Song, W.; Strack, R. L.; Thorn, A.; Jaffrey, S. R.; Ferré-D'Amaré, A. R. Structural Basis for Activity of Highly Efficient RNA Mimics of Green Fluorescent Protein. *Nat Struct Mol Biol* **2014**, *21*, 658–663.

(80) Arsene, A. L.; Uivarosi, V.; Mitrea, N.; Drăgoi, C. M.; Nicolae, A. C. *In Vitro* Studies Regarding The Interaction of Some Novel Ruthenium (III) Complexes with Double Stranded Calf Thymus Deoxyribonucleic Acid (DNA). *Farmacia.* **2016**, *64*, 712–716.

(81) Guan, Y.; Zhou, W.; Yao, X.; Zhao, M.; Li, Y. Determination of Nucleic Acids based on the Fluorescence Quenching of Hoechst 33258 at pH 4.5. *Anal. Chim. Acta* **2006**, *570*, 21–28.

(82) Therrien, B. Transporting and Shielding Photosensitisers by Using Water-Soluble Organometallic Cages: A New Strategy in Drug Delivery and Photodynamic Therapy. *Chem. Eur. J.* **2013**, *19*, 8378–8386.

(83) Schmitt, F.; Freudenreich, J.; Barry, N. P. E.; Juillerat-Jeanneret, L.; Süss-Fink, G.; Therrien, B. Organometallic Cages as Vehicles for Intracellular Release of Photosensitizers. *J. Am. Chem. Soc.* **2012**, *134*, 754–757.

(84) Zheng, Y.-R.; Suntharalingam, K.; Johnstone, T. C.; Lippard, S. J. Encapsulation of Pt(IV) Prodrugs within a Pt(II) Cage for Drug Delivery. *Chem. Sci.* **2015**, *6*, 1189–1193.

(85) Fernández, A.; Vendrell, M. Smart Fluorescent Probes for Imaging Macrophage Activity. *Chem. Soc. Rev.,* **2016**, *45*, 1182–1196.

(86) Ochs, M.; Carregal-Romero, S.; Rejman, J.; Braeckmans, K.; De Smedt, S. C.; Parak, W. J. Light-Addressable Capsules as Caged Compound Matrix for Controlled Triggering of Cytosolic Reactions. *Angew. Chem. Int. Ed.*. **2013**, *52*, 695–699.

(87) Xu, H.; Gao, J.; Jiang, D. Stable, Crystalline, Porous, Covalent Organic Frameworks as a Platform for Chiral Organocatalysts. *Nat. Chem.* **2015**, *7*, 905–912.

(88) Abd El-Mawla, A. M.; Beerhues, L. Benzoic Acid Biosynthesis in Cell Cultures of *Hypericum androsaemum*. *Planta* **2002**, *214*, 727–733.

(89) Lerestif, J. M.; Perrocheau, J.; Tonnard, F.; Bazureau, J. P.; Hamelin, J. 1,3-Dipolar Cycloaddition of Imidate Ylides on Imino-Alcohols: Synthesis of New Imidazolones Using Solvent Free Conditions. *Tetrahedron* **1995**, *51*, 6757–6774.

(90) Williams, D. E.; Dolgopolova, E. A.; Pellechia, P. J.; Palukoshka, A.; Wilson, T. J.; Tan, R.; Maier, J. M.; Greytak, A. B.; Smith, M. D.; Krause, J. A.; Shustova, N. B. Mimic of the Green Fluorescent Protein *β*-Barrel: Photophysics and Dynamics of Confined Chromophores Defined by a Rigid Porous Scaffold. *J. Am. Chem. Soc.* **2015**, *137*, 2223–2226.

(91) Dolgopolova, E. A.; Moore, T. M.; Fellows, W. B.; Smith, M. D.; Shustova, N. B. Photophysics of GFP-Related Chromophores Imposed by a Scaffold Design. *Dalton Trans.* **2016**, *45*, 9884–9891.

(92) Yuan, S.; Lu, W.; Chen, Y.-P.; Zhang, Q.; Liu, T.-F.; Feng, D.; Wang, X.; Qin, J.; Zhou, H.-C. Sequential Linker Installation: Precise Placement of Functional Groups in Multivariate Metal-Organic Frameworks. *J. Am. Chem. Soc.* **2015**, *137*, 3177–3180.

(93) Tsien, R. Y. The Green Fluoresent Protein. *Annu. Rev. Biochem.* **1998**, *67*, 509–544.

(94) Berman, H. M.; Westbrook, J.; Feng, Z.; Gilliland, G.; Bhat, T. N.; Weissig, H.; Shindyalov, I. N.; Bourne, P. E. The Protein Data Bank. *Nucleic Acids Res.* **2000**, *28*, 235–242.

(95) Fujita, M.; Oguro, D.; Miyazawa, M.; Oka, H.; Yamaguchi, K.; Ogura, K. Self-Assembly of Ten Molecules into Nanometre-Sized Organic Host Frameworks. *Nature* **1995**, *378*, 469–471.

(96) Grimme, S.; Antony, J.; Ehrlich, S.; Krieg, H. A Consistent and Accurate ab initio Parametrization of Density Functional Dispersion Correction (DFT-D) for the 94 Elements H-Pu. *J. Chem. Phys.* **2010**, *132*, 154104.

(97) Jacquemin, D. Excited-State Dipole and Quadrupole Moments: TD-DFT versus CC2. *J. Chem. Theory Comput.* **2016**, *12*, 3993–4003.

(98) Shao, Y.; Gan, Z.; Epifanovsky, E.; Gilbert, A. T. B.; Wormit, M.; Kussmann, J.; Lange, A. W.; Behn, A.; Deng, J.; Feng, X.; Ghosh, D.; Goldey, M.; Horn, P. R.; Jacobson, L. D.; Kaliman, I.; Khaliullin, R. Z.; Kus, T.; Landau, A.; Liu, J.; Proynov, E. I.; Rhee, Y. M.; Richard, R. M.; Rohrdanz, M. A.; Steele, R. P.; Sundstrom, E. J.; Woodcock, H. L.; Zimmerman, P. M.; Zuev, D.; Albrecht, B.; Alguire, E.; Austin, B.; Beran, G. J. O.; Bernard, Y. A.; Berquist, E.; Brandhorst, K.; Bravaya, K. B.; Brown, S. T.; Casanova, D.; Chang, C.-M.; Chen, Y.; Chien, S. H.; Closser, K. D.; Crittenden, D. L.; Diedenhofen, M.; DiStasio, R. A.; Do, H.; Dutoi, A. D.; Edgar, R. G.; Fatehi, S.; FustiMolnar, L.; Ghysels, A.; Golubeva-Zadorozhnaya, A.; Gomes, J.; Hanson-Heine, M. W. D.; Harbach, P. H. P.; Hauser, A. W.; Hohenstein, E. G.; Holden, Z. C.; Jagau, T.-C.; Ji, H.; Kaduk, B.; Khistyaev, K.; Kim, J.; Kim, J.; King, R. A.; Klunzinger, P.; Kosenkov, D.; Kowalczyk, T.; Krauter, C. M.; Lao, K. U.; Laurent, A. D.; Lawler, K. V.; Levchenko, S. V.; Lin, C. Y.; Liu, F.; Livshits, E.; Lochan, R. C.; Luenser, A.; Manohar, P.; Manzer, S. F.; Mao, S.-P.; Mardirossian, N.; Marenich, A. V.; Maurer, S. A.; Mayhall, N. J.; Neuscamman, E.; Oana, C. M.; Olivares-Amaya, R.; O'Neill, D. P.; Parkhill, J. A.; Perrine, T. M.; Peverati, R.; Prociuk, A.; Rehn, D. R.; Rosta, E.; Russ, N. J.; Sharada, S. M.; Sharma, S.; Small, D. W.; Sodt, A.; Stein, T.; Stück, D.; Su, Y.-C.; Thom, A. J. W.; Tsuchimochi, T.; Vanovschi, V.; Vogt, L.; Vydrov, O.; Wang, T.; Watson, M. A.; Wenzel, J.; White, A.; Williams, C. F.; Yang, J.; Yeganeh, S.; Yost, S. R.; You, Z.-Q.; Zhang, I. Y.; Zhang, X.; Zhao, Y.; Brooks, B. R.; Chan, G. K. L.; Chipman, D. M.; Cramer, C. J.; Goddard, W. A.; Gordon, M. S.; Hehre, W. J.; Klamt, A.; Schaefer, H. F.; Schmidt, M. W.; Sherrill, C. D.; Truhlar, D. G.; Warshel, A.; Xu, X.; Aspuru-Guzik, A.; Baer, R.; Bell, A. T.; Besley, N. A.; Chai, J.-D.; Dreuw, A.; Dunietz, B. D.; Furlani, T. R.; Gwaltney, S. R.; Hsu, C.-P.; Jung, Y.; Kong, J.; Lambrecht, D. S.; Liang, W.; Ochsenfeld, C.; Rassolov, V. A.; Slipchenko, L. V.; Subotnik, J. E.; Van Voorhis, T.; Herbert, J. M.; Krylov, A. I.; Gill, P. M. W.; Head-Gordon, M. Advances in Molecular Quantum Chemistry Contained in the Q-Chem 4 Program Package. *Mol. Phys.* **2015**, *113*, 184−215.

(99) Shao, Y.; Molnar, L.F.; Jung, Y.; Kussmann, J.; Ochsenfeld, C.; Brown, S. T.; Gilbert, A. T. B.; Slipchenko, L. V.; Levchenko, S. V.; O'Neill, D. P.; DiStasio Jr, R. A.; Lochan, R. C.; Wang, T.; Beran, G. J. O.; Besley, N. A.; Herbert, J. M.; Lin, C. Y.; Van Voorhis, T.; Chien, S. H.; Sodt, A.; Steele, R. P.; Rassolov, V. A.; Maslen, P. E.; Korambath, P. P.; Adamson, R. D.; Austin, B.; Baker, J.; Byrd, E. F. C.; Dachsel, H.; Doerksen, R. J.; Dreuw, A.; Dunietz, B. D.; Dutoi, A. D.; Furlani, T. R.; Gwaltney, S. R.; Heyden, A.; Hirata, S.; Hsu, C.-P.; Kedziora, G.; Khalliulin, R. Z.; Klunzinger, P.; Lee, A. M.; Lee, M. S.; Liang, W.; Lotan, I.; Nair, N.; Peters, B.; Proynov, E. I.; Pieniazek, P. A.; Rhee, Y. M.; Ritchie, J.; Rosta, E.; Sherrill, C. D.; Simmonett, A. C.; Subotnik, J. E.; Woodcock III, H. L.; Zhang, W.; Bell, A. T.; Chakraborty, A. K.; Chipman, D. M.; Keil, F. J.; Warshel, A.; Hehre, W. J.; Schaefer III, H. F.; Kong, J.; Krylov, A. I.; Gill P. M. W.; Head-Gordon, M. Advances in Methods and Algorithms in a Modern Quantum Chemistry program Package. *Phys. Chem. Chem. Phys.*, **2006**, *8*, 3172−3191.

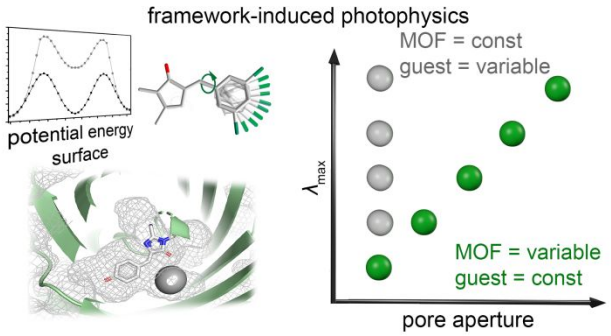
framework-induced photophysics
potential energy surface
MOF = const
guest = variable
MOF = variable
guest = const
λ_{max}
pore aperture

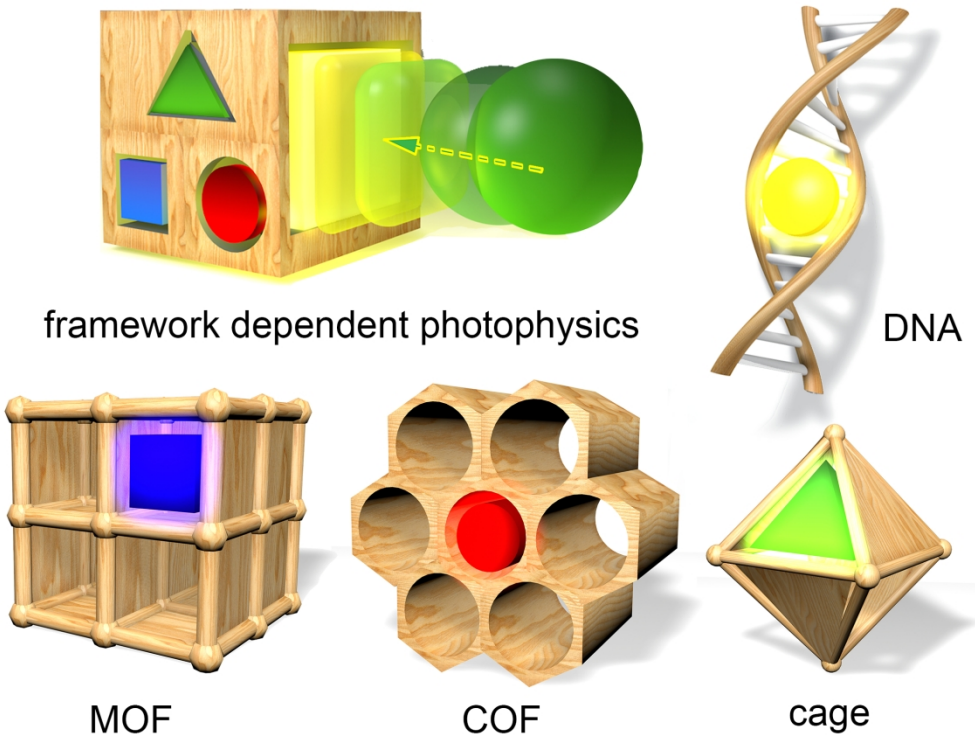

Scheme 1

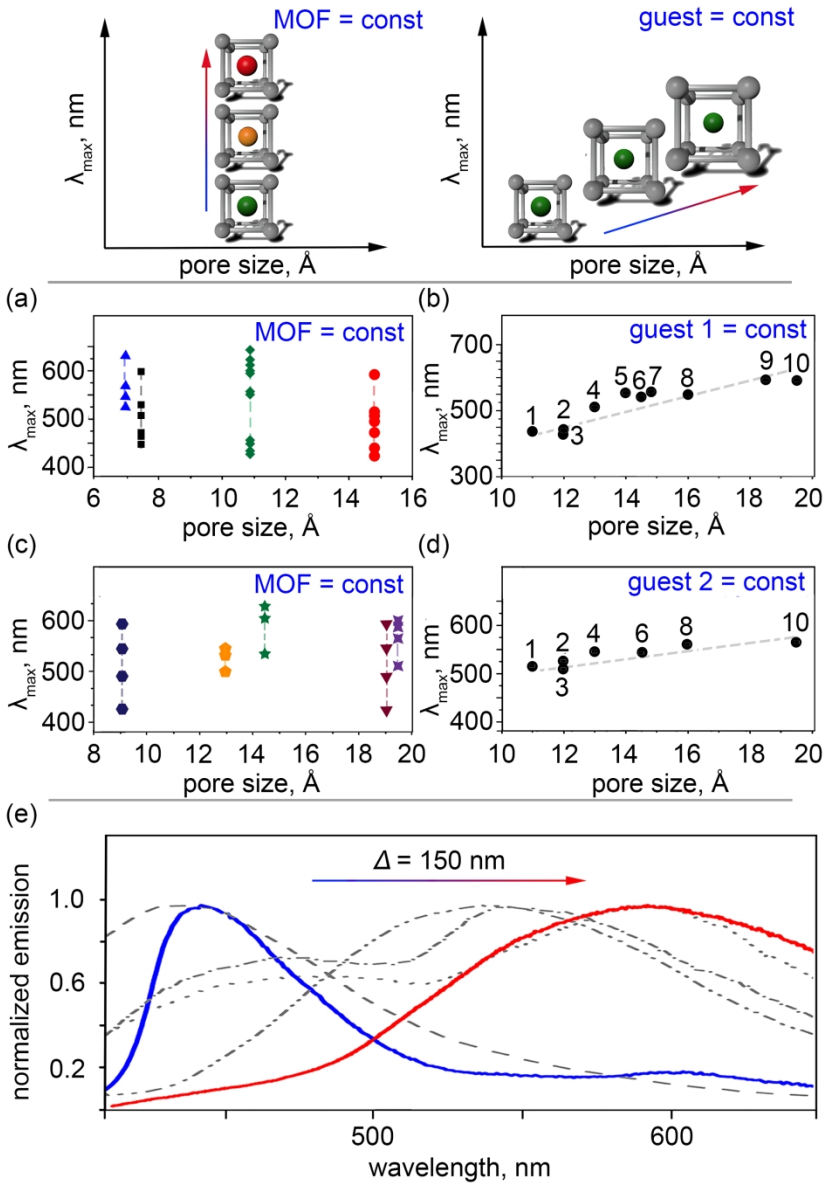
MOF = const
guest = const
λmax, nm
pore size, Å
(a)
(b)
(c)
(d)
(e)
guest 1 = const
guest 2 = const
Δ = 150 nm
normalized emission
wavelength, nm

Figure 1

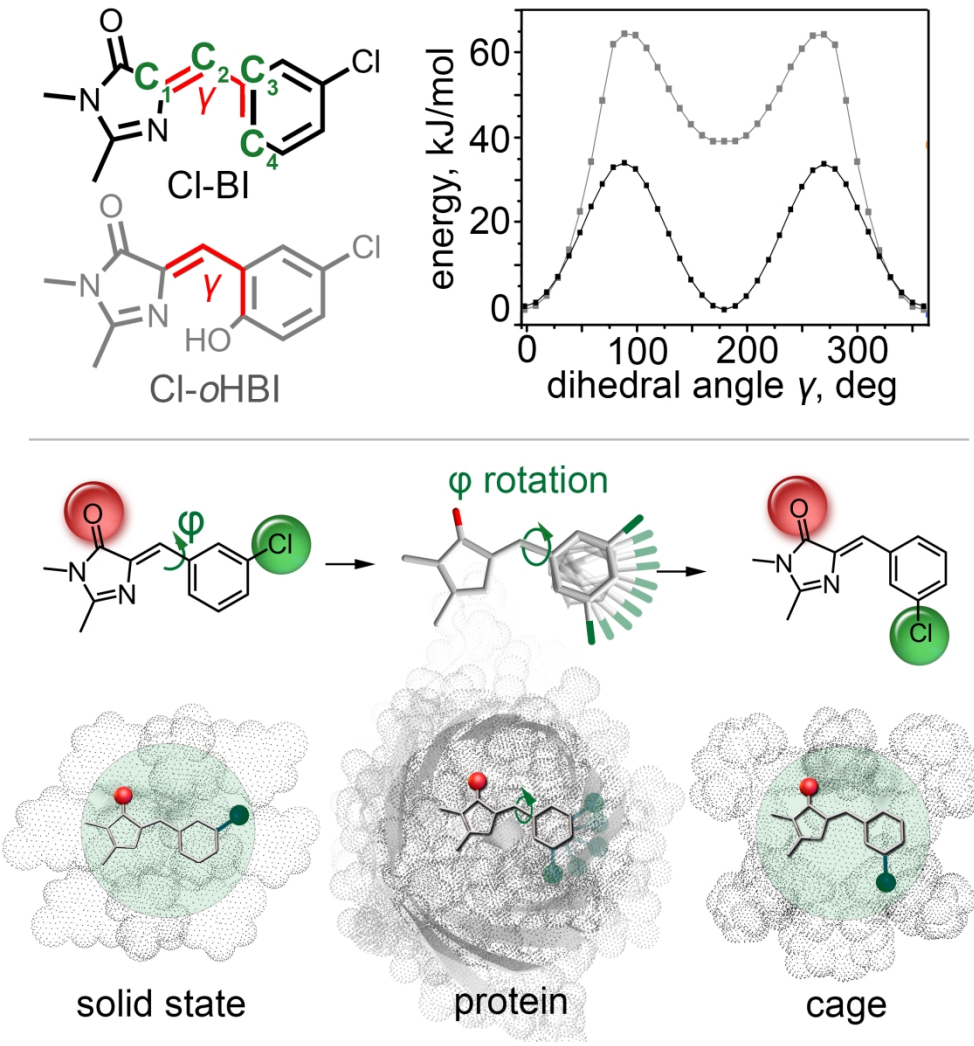
Cl-BI
Cl-oHBI
energy, kJ/mol
dihedral angle γ, deg
φ rotation
solid state
protein
cage

Figure 2

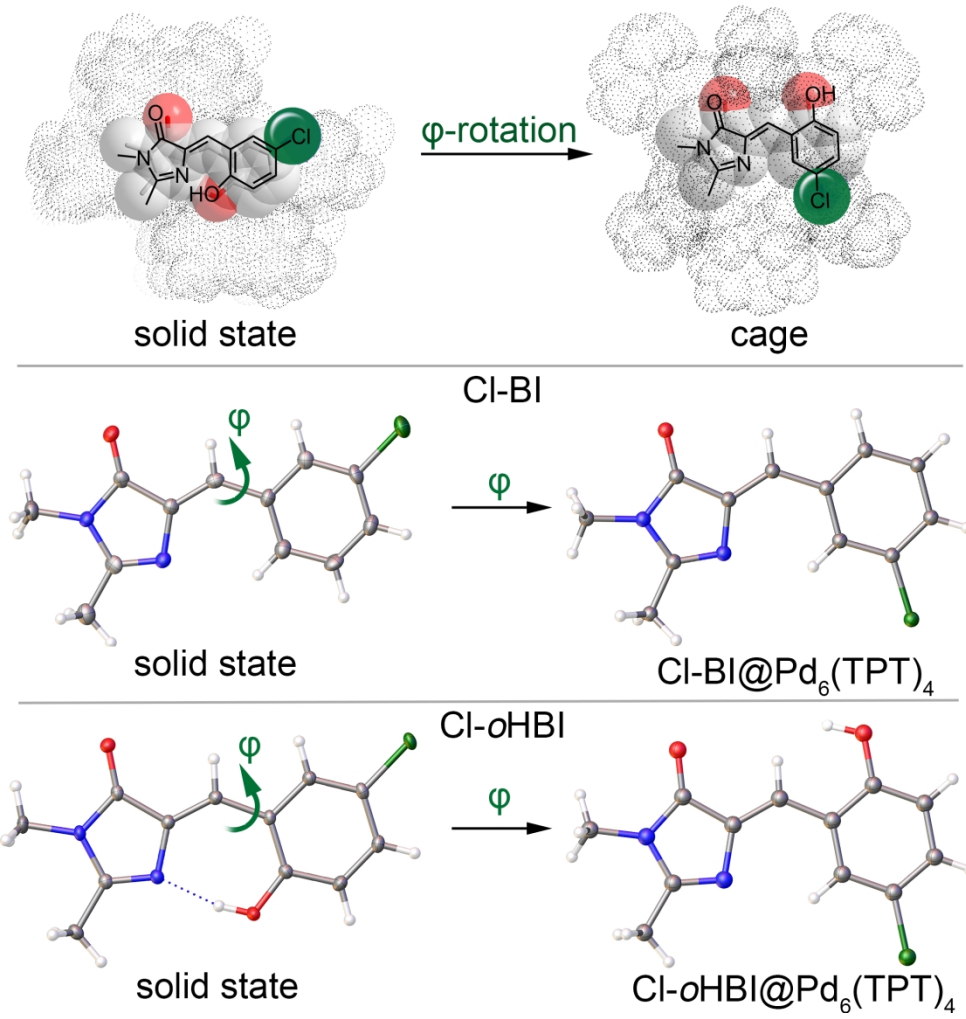
φ-rotation
solid state
cage
Cl-BI
φ
solid state
Cl-BI@Pd6(TPT)4
Cl-oHBI
φ
solid state
Cl-oHBI@Pd6(TPT)4

Figure 3

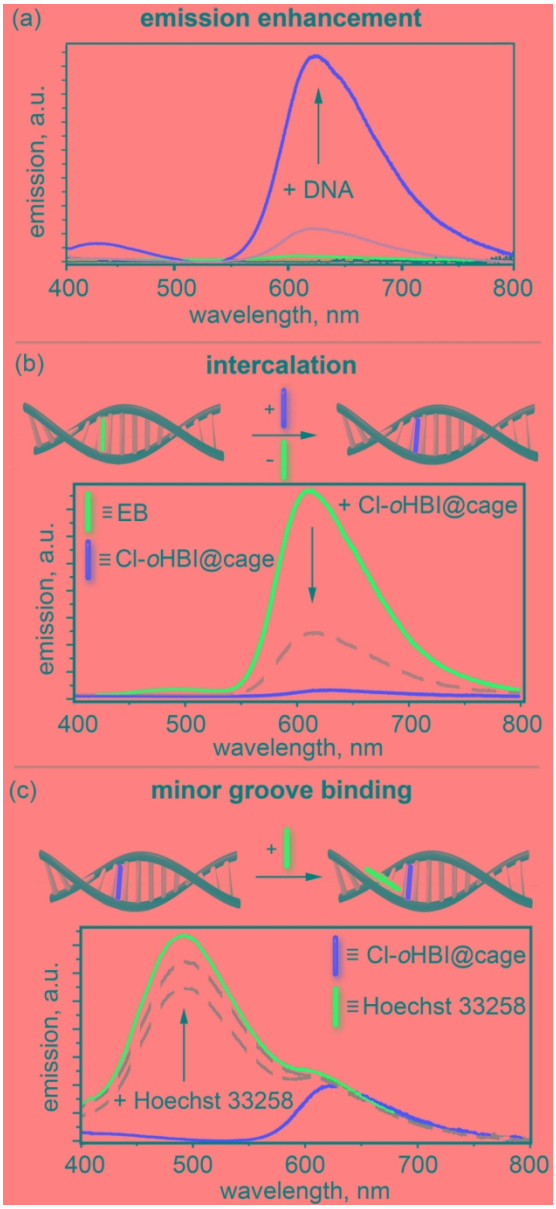
(a)
emission enhancement
emission, a.u.
+ DNA
400
500
600
700
800
wavelength, nm
(b)
intercalation
+
-
≡ EB
≡ Cl-oHBI@cage
+ Cl-oHBI@cage
emission, a.u.
400
500
600
700
800
wavelength, nm
(c)
minor groove binding
+
≡ Cl-oHBI@cage
≡ Hoechst 33258
emission, a.u.
+ Hoechst 33258
400
500
600
700
800
wavelength, nm

Figure 4

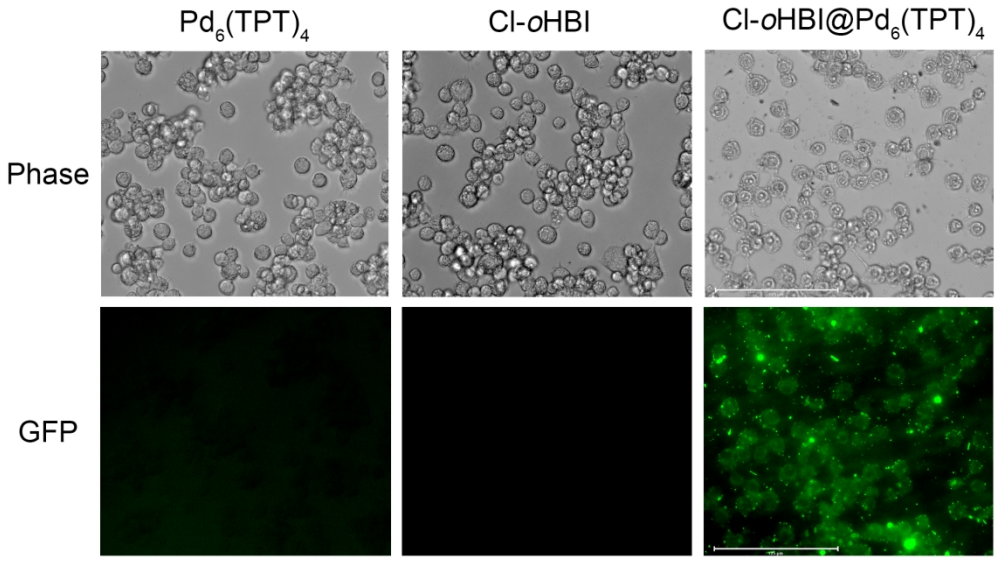

Figure 5

83x49mm (700 x 700 DPI)

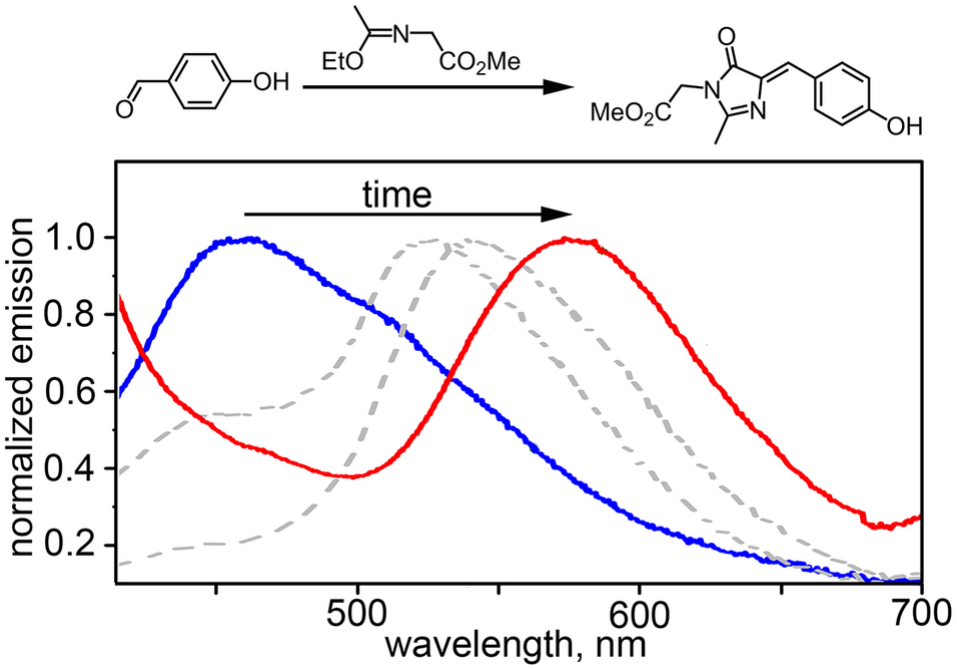

Figure 6

84x56mm (300 x 300 DPI)

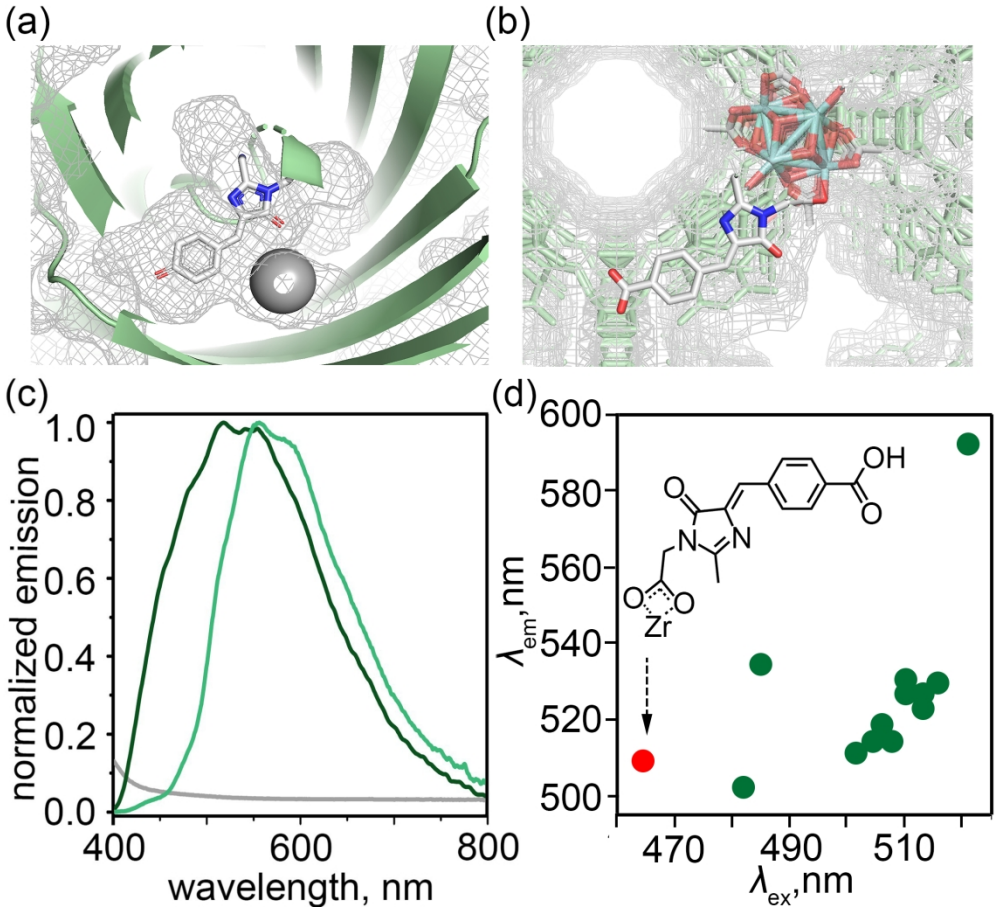
(a)
(b)
(c)
(d)
normalized emission
1.0
0.8
0.6
0.4
0.2
0.0
400
600
800
wavelength, nm
600
580
560
540
520
500
λ_{em},nm
470
490
510
λ_{ex},nm
OH
O
N
N
O
O
Zr

Figure 7

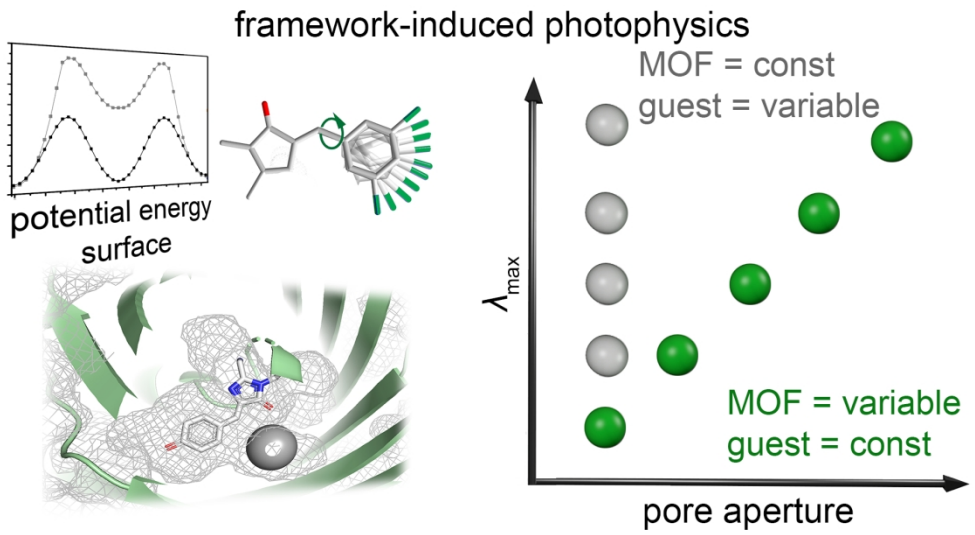
framework-induced photophysics
potential energy surface
MOF = const
guest = variable
MOF = variable
guest = const
λ_{max}
pore aperture

TOC